

Supplementary Information

**A 3D-printed hierarchical chimney for high-yield solar evaporation**

Yu Tang,<sup>‡a,b</sup> Chenyi Fang,<sup>‡c</sup> Xin Xu,<sup>d</sup> Feng Li,<sup>c</sup> Lei Fan,<sup>a</sup> Di Zhu,<sup>b</sup> Jun Ding,<sup>d</sup> Joseph Imbrogno,<sup>e</sup> Sui Zhang\*<sup>c</sup> and Wentao Yan\*<sup>a</sup>

<sup>a</sup> Department of Mechanical Engineering, National University of Singapore, 117575, Singapore

<sup>b</sup> College of Mechanical and Electrical Engineering, Nanjing University of Aeronautics and Astronautics, Nanjing, 210016, China

<sup>c</sup> Department of Chemical and Biomolecular Engineering, National University of Singapore, 117580, Singapore

<sup>d</sup> Department of Materials Science and Engineering, National University of Singapore, 117575, Singapore

<sup>e</sup> Chemical Research & Development, Pfizer Inc., 280 Shennecossett Rd, Groton, CT 06340, USA

\* Corresponding authors: [chezhasu@nus.edu.sg](mailto:chezhasu@nus.edu.sg), [mpeyanw@nus.edu.sg](mailto:mpeyanw@nus.edu.sg)

<sup>‡</sup> Yu Tang and Chenyi Fang contributed equally to this work.

## S1. Geometric configuration of CPCGG

The chimney fabricated by porous CA-GO strut with bottom-to-up channel (CPCGG) is presented in Fig. S1. The CPCGG has a hollow cylindrical structure, with two side-holes located at the bottom and bottom-to-up gas channel in the middle. CPCGG has a height ( $H$ ) of 55 mm with an outside diameter ( $D$ ) of 8.5 mm and inside diameter ( $d$ ) of 3 mm. The two side holes have a size of 1.6 mm, and the distance between these side holes and top surface of CPCGG ( $L$ ) is 45 mm. The size of micro-cell of the open-cell architecture inside chimney is 0.45 mm.

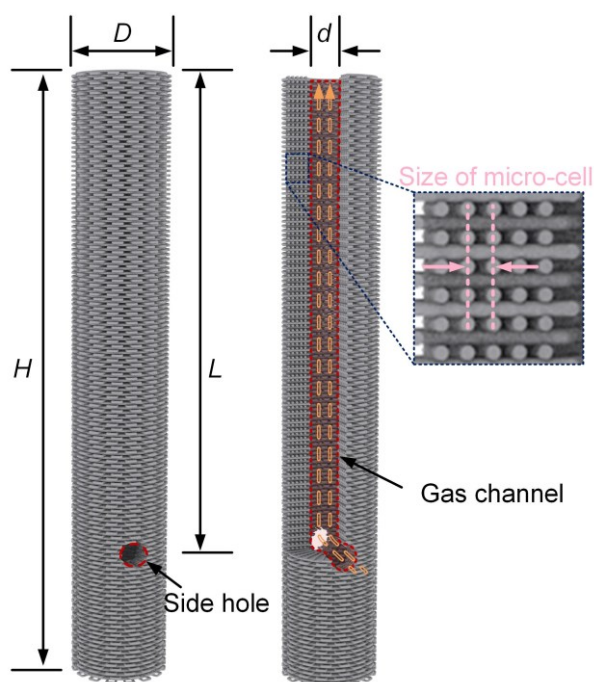


**Fig. S1** Structural illustration and SEM images of CPCGG.

## S2. Inks for 3D printing

In this work, three different inks were prepared for 3D-printing, including CA+EA, CA+EA+GO, and CA+EA+GO+Water. Therefore, three different struts could be printed by these inks, including CA, CA-GO and porous CA-GO (Fig. S2a). Meanwhile, four types of chimney were fabricated by these inks and corresponding strut, including the chimney fabricated by CA strut (CCA), the chimney fabricated by CA-GO strut (CCG), the chimney fabricated by porous CA-GO strut (CPCG), and the chimney fabricated by the porous CA-GO strut with gas channel (CPCGG). Details of their compositions as well as the struts and chimneys derived from them are summarized in Table S1. In our 3D printing process, the solvent (ethyl acetate, EA) evaporates to cure the printed sample. When graphene oxide (GO)

is incorporated into the ink, it impedes the evaporation of EA, thereby slowing the curing process. To compensate for this reduced curing speed and ensure timely solidification, an increased amount of CA is necessary when GO is present in the ink to enhance the solid content and accelerate the curing speed. Conversely, in the CCA samples where GO is absent, EA evaporates more rapidly, leading to a faster curing rate. While advantageous for the curing process, an overly rapid curing rate poses a risk of clogging the printer nozzle, potentially disrupting the printing process. To mitigate this risk and ensure a smooth and continuous printing process, the CA content in CCA samples is deliberately reduced. This adjustment is a practical measure to balance the curing speed against the operational requirements of our 3D printing technique, ensuring that printing can proceed without interruption.

The rheological properties of these 3D-printing ink were characterized using both steady shear and oscillatory modes on a modular advanced rheometer (Haake™ Mars™, Thermo Scientific™, USA) at 25 °C using a 40 mm dual Peltier plate. Apparent viscosity was recorded as a function of shear rate using a logarithmically ascending series. The storage modulus ( $G'$ ) and loss modulus ( $G''$ ) were measured as functions of oscillatory stress ( $1\sim 10^4$  Pa) at a constant angular frequency of  $6.283\text{ rad s}^{-1}$ . The rheological properties of three different inks are shown in Figs. S2b and S2c. An excellent 3D-printing ink should possess ideal rheological behaviour, in which the viscosity and modulus would drop at high shear rate. These inks showed similar shear-thinning behaviours when the shear rate increased from 1 to  $100\text{ s}^{-1}$ , and a high self-standing yield stress in the order of  $10^3$  when the shear rate was  $\sim 1\text{ s}^{-1}$  (Fig. S2b). The following test proved that the elasticity ( $G' > G''$ ) transition to viscosity ( $G'' > G'$ ) was quasi-instantaneous immediately after shear stress surpassed the flow stress ( $\tau_f$ ), where the ink would yield and be able to flow so that it could be extruded out of the 3D-printing nozzle (Fig. S2c). The pneumatic air pressure of the 3D-printing system provided a shear stress level above  $\tau_f$  for extrusion to take place. After extrusion, the extruded strut would retain its shape due to the elimination of pressure and high self-standing yield stress (Figs. S2b and S2c), so that the structural integrity of the printed material could be preserved.

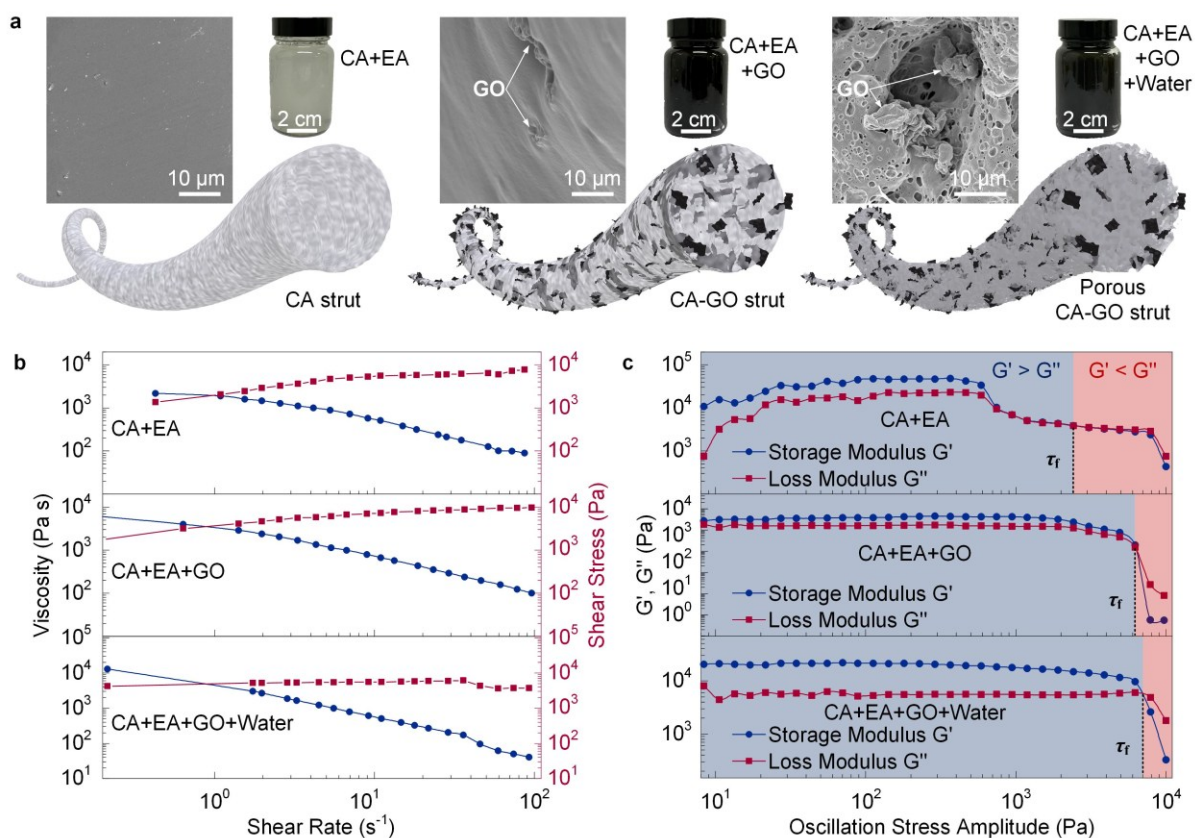


**Fig. S2** 3D-printing inks and their rheological properties. (a) SEM images and schematics of CA, CA-GO, and porous CA-GO strut. Photos of their respective inks. (b) Plot of apparent viscosity and shear stress as a function of shear rates. (c) Stress amplitude sweep plot at a constant frequency of 6.283 rad/s.

**Table S1.** Composition of inks as well as fibres and chimneys derived from them.

Chimney	Ink	Type of strut	Composition			
			EA	CA	GO	Water
CCA	CA+EA	CA	100 g	42 g	-	-
CCG	CA+EA+GO	CA-GO	100 g	44 g	1 g	-
CPCG	CA+EA+GO+water	Porous CA-GO	100 g	44 g	1 g	10 g
CPCGG	CA+EA+GO+water	Porous CA-GO	100 g	44 g	1 g	10 g

### S3. Chemical compositions

The attenuated total reflectance-Fourier-transform infrared (ATR-FTIR) spectrum indicates that there is a broad peak observed at 3500~3350 cm<sup>-1</sup> for both CA and GO, which is attributed to hydroxyl (-OH) groups (Fig. S3). The X-ray photoelectron spectroscopy (XPS) analysis is

also used to further characterize the chemical states of various elements and identify functional groups in CA powder and GO nanosheet. Fig. S4a shows high-resolution XPS spectra of C 1s region in CA powder. The deconvoluted C 1s peaks shows peak binding energies of 287.3 and 284.8 eV, which correspond to C=O, C-C bonds, respectively.<sup>1</sup> The peak at 283.4 eV is ascribed to methyl carbon of the acetyl groups [H<sub>3</sub>C(C=O)].<sup>2</sup> The peak at 286.3 eV is associated with C-O bonds, which is mainly attributed to the hydroxyl (-OH) groups around the cyclic glucose molecules<sup>1</sup>. The chemical state of oxygen element on the surface of GO powder is displayed in the high-resolution XPS spectra of O 1s region (Fig. S4b). Peaks at 533.9, 532.63 and 531.30 eV represent the C-O-C, C-OH, and C=O groups, respectively.<sup>3</sup> The analysis results indicate the hydrophilic nature of CA and GO.

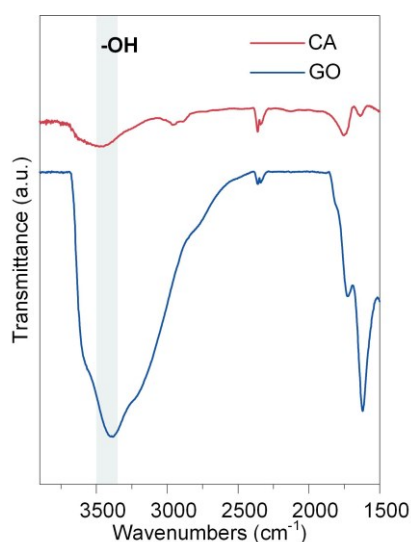


**Fig. S3** ATR-FTIR spectra of CA and GO.

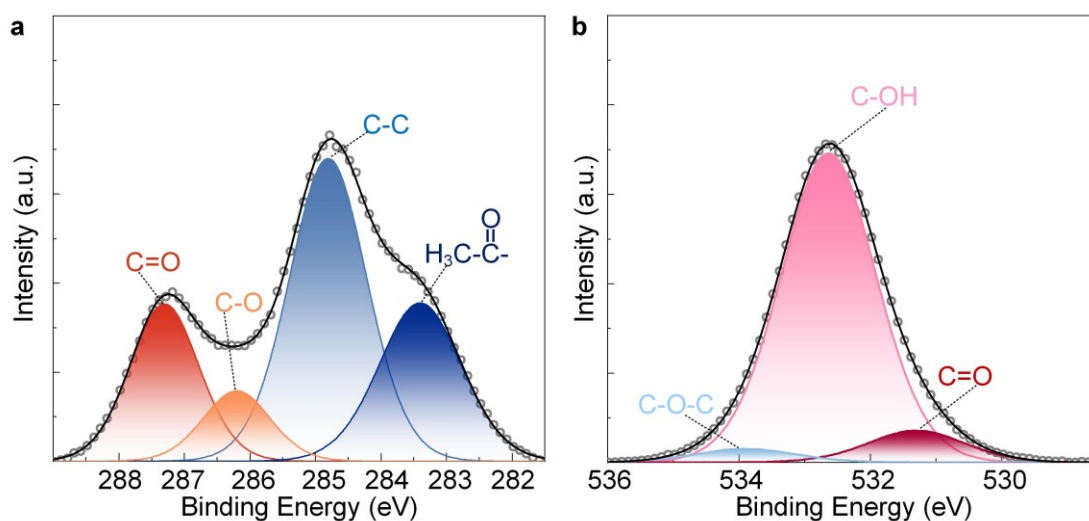


**Fig. S4** XPS analysis. (a) Typical high-resolution XPS spectra of C 1s region of CA. (b) Typical high-resolution XPS spectra of O 1s region of GO.

#### S4. Construction of hierarchical chimney

The surfaces of CA and GO are rich in hydroxyl (-OH) groups, which results in a strong hydrogen-bonding network with water in the 3D-printing ink composed of CA+EA+GO+Water. In this particular ink, water molecules penetrate into the CA-EA solution through hydrogen bonding, and they strongly adsorb to the hydrophilic groups on the surface of CA and GO, especially hydroxyl groups (-OH, see Section S2 and Figs. S3 and S4). Thereafter, water molecules in the form of nano-film and micro-droplet act as scissors to cut CA clusters, as well as to separate the CA from the GO (Fig. S5). After EA and water are removed from the matrix during subsequent process, the porous CA backbone is obtained. GO nano-sheets are connected with CA substrate by micro-cavities and nano-channels inside the porous CA-GO strut.

The transmission electron microscopy (TEM) images (Fig. S6) illustrates that CA contacts with edges of GO, without intrusion into the inner structure of GO nano-sheet, and the folded inner surface of GO is not covered by any CA. Therefore, the water supply could easily reach the outer surface of GO, as well as through these nano-gaps to every corner of the folded GO beneath the outer surface, ensuring effective water supply to photo-thermal interface.

The surfaces of CA and CA-GO samples are hydrophilic, and they exhibit water contact angles of  $24.6^\circ$  and  $33.6^\circ$ , respectively (Fig. S6). On the other hand, the droplet would penetrate into the interior of the porous CA-GO surface under the action of strong capillary force. Thin liquid films are immediately formed in micro cavities and nano-channels, leading to super-hydrophilicity (Fig. S7). Contact angle measurements were performed using an optical contact angle system (OCA25, DataPhysics, Germany) *via* the sessile drop method, in which a  $2\ \mu\text{L}$  water droplet was gently dispersed onto the material surface.

The pore size distribution and porosity of three material types, including CA, CA-GO, and porous CA-GO, have been quantified *via* using a mercury porosimeter (AutoPore V 9600). The experimental results show that CA and CA-GO exhibit porosities of 4.9% and 5.0%, respectively, with all pores being less than 500 nm in diameter. These pores in CA and CA-GO are primarily mesopores, with dominant pore diameters of approximately 7 nm and 11 nm, respectively (Figs. S8a and S8b). In contrast, porous CA-GO exhibits a broader pore size distribution ranging from 5 nm to  $20\ \mu\text{m}$  (Fig. S8c), with a higher overall porosity of 9.4%.

To investigate the functional role of the hierarchical porosity in porous CA-GO, we evaluated the water transport behavior by observing the spreading and infiltration dynamics of  $2\ \mu\text{L}$  water droplets placed on the surfaces of CA-GO and porous CA-GO. Time-resolved imaging reveals

that droplets on porous CA-GO rapidly infiltrate into the internal porous network (Fig. S9a), indicating efficient capillary-driven transport facilitated by interconnected micro- and mesopores. In contrast, droplets on CA-GO remain on the surface without appreciable penetration (Fig. S9b), suggesting limited permeability. These findings confirm that the enlarged porosity and hierarchical pore structure of porous CA-GO enhance direct water supply, which is essential for sustaining capillary-driven evaporation in solar thermal applications.

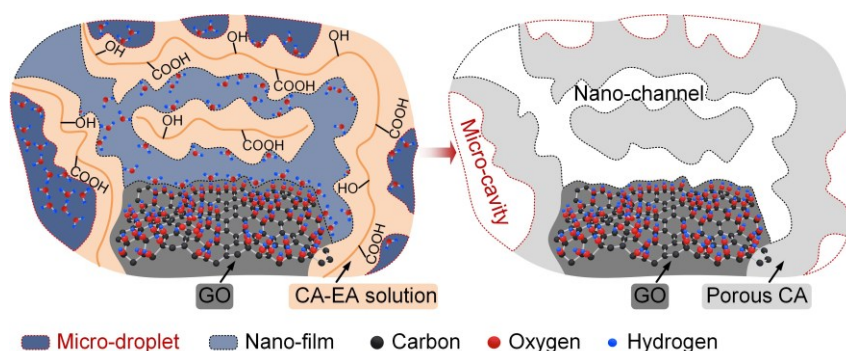


**Fig. S5** Schematic illustration of the generation of micro-cavity and nano-channel inside the strut.

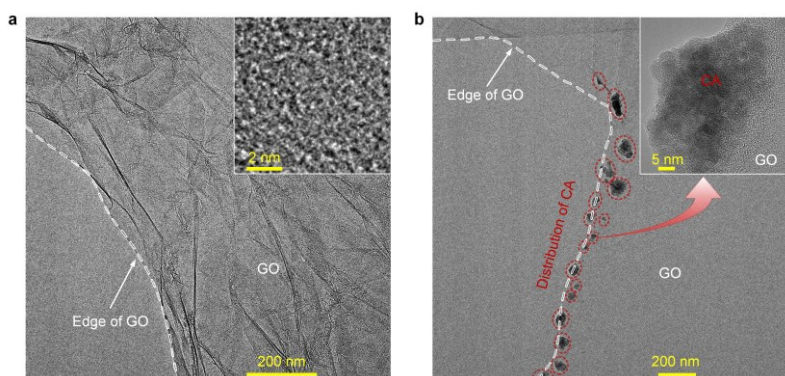


**Fig. S6** TEM images of GO nano-sheet and the GO wrapped in porous CA-GO strut. (a) GO nano-sheet. (b) The GO wrapped in porous CA-GO strut.

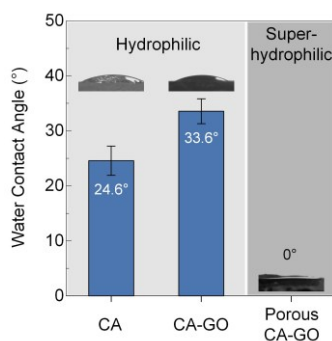


**Fig. S7** Water contact angles of the printed CA, CA-GO, and porous CA-GO flat sheet.

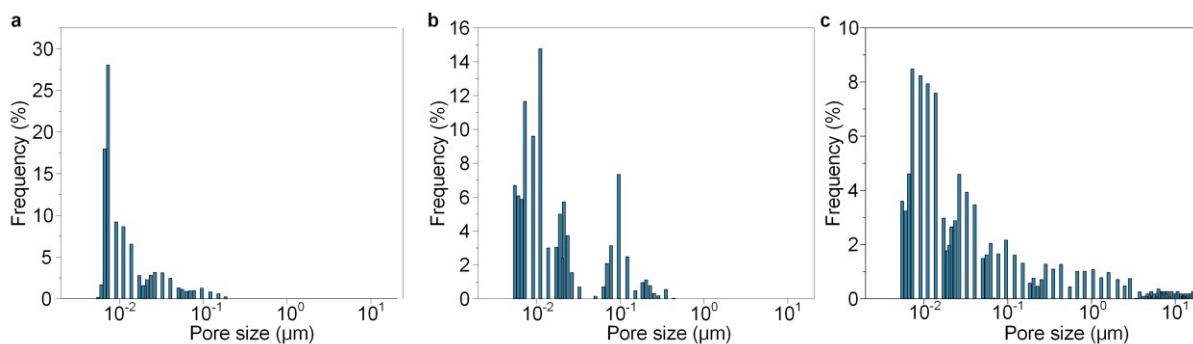


**Fig. S8** Pore size distribution of different materials. (a) CA. (b) CA-GO. (c) Porous CA-GO.

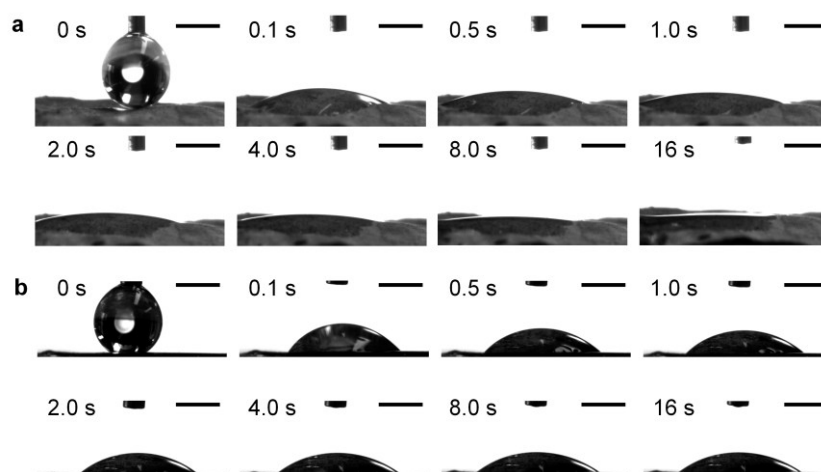


**Fig. S9** Time-lapse images of 2  $\mu\text{L}$  water droplet spreading and infiltration on two different material surfaces. (a) Porous CA-GO. The droplet rapidly infiltrates into the porous network. (b) CA-GO. The droplet remains on the surface without significant penetration. The scale bar is 500  $\mu\text{m}$ .

## S5. Geometric configuration of cuboid chimneys

Three different types of chimneys (CCA, CCG and CPCG) have the cuboid contour (Fig. S10), where the chimney effect only occurred on their outer surface. They are also composed of the micro-cells of open-cell architecture with pre-determined size (Fig. S11). After immediate post-treatment of chimneys constructed from 3D printing process, they were stored in deionized water at room conditions upon further usage. The geometric dimension (including, height  $H$ , width  $W_1$  and thickness  $W_2$ ), micro-cell size of the open-cell architecture, and types of fibre of these chimneys are shown in Table S2. For these samples with the micro-cell size of 0.45 mm, the shrinkage of the printed structure increases with the volatilization of ethyl acetate during the curing process, thus the overall cross-section size of these samples is reduced to 9 mm  $\times$  9 mm.

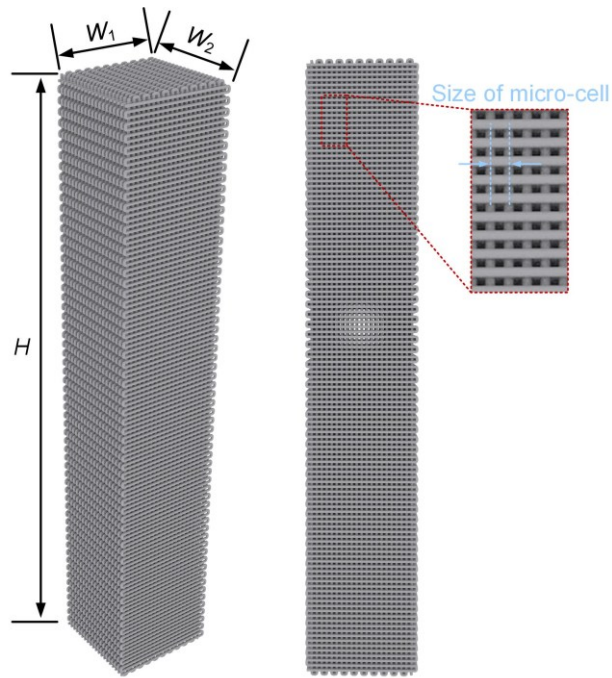


**Fig. S10** Structures of CCA, CCG and CPCG.

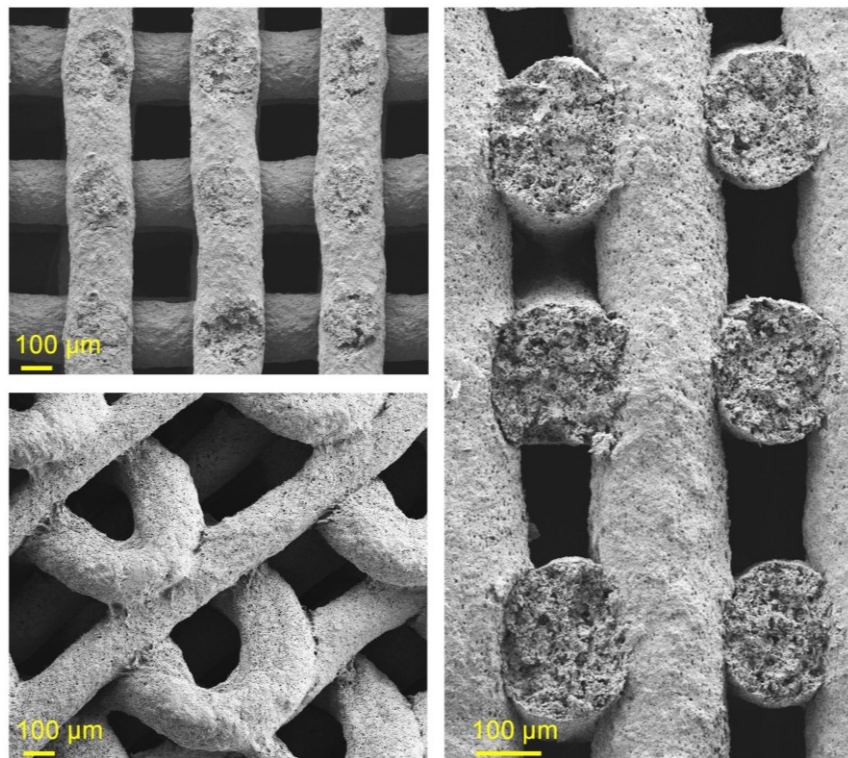


**Fig. S11** SEM images of CPCG. Figure on the upper left corner refers to micro-cell of the open-cell architecture. Figure on the lower left is the side view of CPCG. Figure on the right represent the cross section of strut.

**Table S2.** Dimensional parameters of cuboid chimneys.

Chimney	Fibre Type	$H \times W_1 \times W_2$	Micro-cell Size
	CA	55×10×10 mm	1.7 mm
CCA	CA	55×9×10 mm	0.9 mm
	CA	55×9×9 mm	0.45 mm
CCG	CA-GO	55×9×9 mm	0.45 mm
CPCG	Porous CA-GO	55×9×9 mm	0.45 mm

**S6. Solar evaporation test**

To efficiently harvest solar energy, high-power concentrators are typically employed to intensify the light concentration on the surface of the solar evaporator, focusing a broad area of sunlight into a small diameter spot.<sup>4-6</sup> In this study, the conditions simulating 3-Sun irradiation with 30 mm spots were examined. The 3-Sun illumination was provided by a solar simulator, and a light blocking frame was placed beneath the solar simulator. It was used to control the light spot with a diameter of 30 mm, where the illumination flux on the top surface of 3D printed chimney was kept at 3 kW/m<sup>2</sup> (Fig. S12). Bulk water was contained in a glass beaker. The 3D printed chimney was floated on the surface of the bulk water by tightly positioning it in one layer of aluminium foil (which also shields the bulk water surface from evaporation). Bottom of chimney was soaked in bulk water to ensure sufficient water transportation to the top of evaporator *via* efficient capillary pumping. Evaporation rate was carefully computed by the following formula:

$$\dot{m} = \frac{\Delta m}{A \cdot t} \quad (\text{SE 1})$$

where  $\dot{m}$  (kg m<sup>-2</sup> h<sup>-1</sup>) refers to evaporation rate,  $\Delta m$  (kg) is the mass change (measured by high precision molecular balance (GR-200, A&D, Japan) in certain time period,  $A$  (m<sup>2</sup>) is the top area of the evaporator and  $t$  (h) is the time of experiment. In this study, each experiment time is 1 h. Three experiments were conducted and the average value was calculated as water evaporation rate.

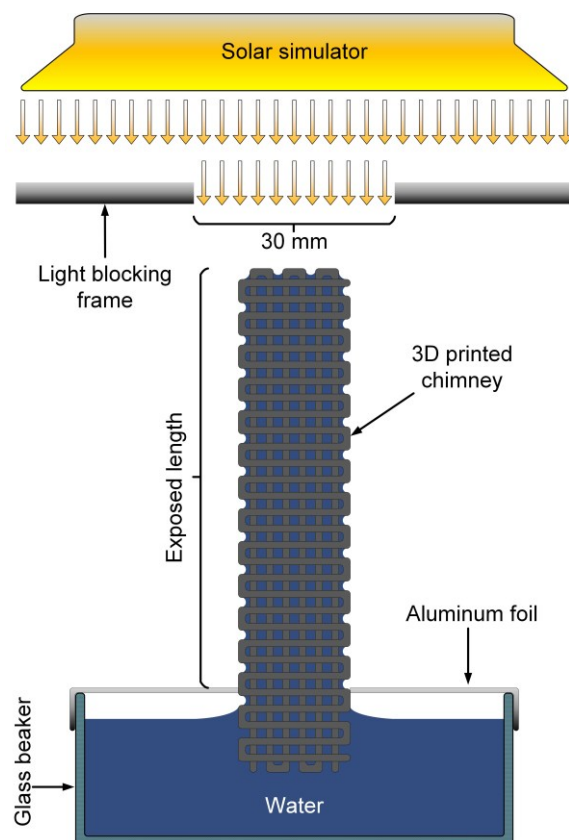


**Fig. S12** Illustration of solar evaporation setup.

### **S7. Optimization of micro-cell dimension of the open-cell architecture**

Taking advantage of the transparent nature of cellulose, the CCA chimney was printed with different open-cell size to observe the water-holding capacities validated by indigo carmine solution (800ppm dissolved in water). For the CCA with the open-cell size of 0.45 mm, it shows the best the water-holding capacity, because all open-cells can withdraw and store water. However, when the open-cell size is 0.9 mm, only 55% of these open-cell can hold water. Once the open-cell size further increases to 1.7 mm, this ratio of the open-cell height filled with water decrease to 26% (Fig. S13).

The as-prepared chimney should float on the surface of the bulk water by positioning it in aluminium foil, and the micro-cells of the open-cell architecture in the chimney must supply water to the evaporation front against downward gravitational force. When the micro-cell size of CCA is 0.45 mm and the exposed length is 50 mm, the solar evaporation rate is the highest ( $5.9 \text{ kg m}^{-2} \text{ h}^{-1}$ ), due to the best water-holding capacity and the highest exposed length. Therefore, the optimal open-cell size of the chimney is 0.45 mm to enable adequate water supply to the evaporation front.

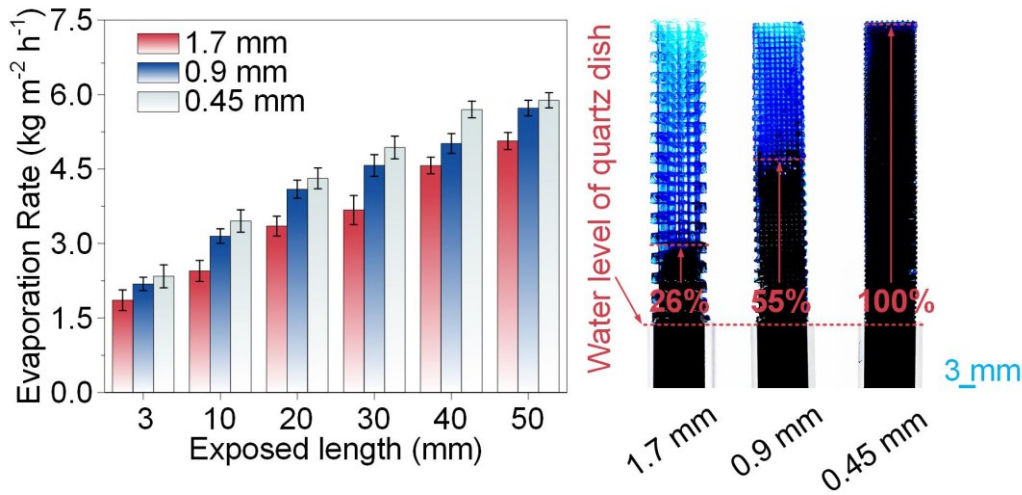


**Fig. S13** Water-holding capacities. Figure on the left indicates the evaporation rates of CCA with different open-cell sizes and exposed length under 3-sun irradiation. 3-Sun = 3 kW m<sup>-2</sup>. Figure on the right represents water-lifting ability of evaporators with different micro-cell sizes against dye solution.

### S8. Effect of exposed length on evaporation performance

Three different types of respective chimneys are printed to examine the effect of exposed length on the solar evaporation rate, including CPCG, CCG, and CCA. The results show that there is a monotonical enhancement in evaporation rate when exposed length increases from 3 mm to 50 mm (Fig. S14). The results point out that, when the exposed length increase from 3 mm to 50 mm, the solar evaporation rate improves from 2.3 kg m<sup>-2</sup> h<sup>-1</sup>, 5.1 kg m<sup>-2</sup> h<sup>-1</sup> and 5.3 kg m<sup>-2</sup> h<sup>-1</sup> to 5.9 kg m<sup>-2</sup> h<sup>-1</sup>, 10.0 kg m<sup>-2</sup> h<sup>-1</sup> and 10.9 kg m<sup>-2</sup> h<sup>-1</sup> for CCA, CCG and CPCG, respectively (Fig. S14).

The highest solar evaporation rate is achieved by CPCG at the exposed length of 50 mm, attributing to the chimney effect, good solar absorption capacity and the network of the micro-cavity and nano-channel inside its porous CA-GO strut where water is supplied directly to the photo-thermal conversion interface between GO nano-sheets and thin water film. Therefore, the final sample exposed height is set at 50 mm for all experiments.

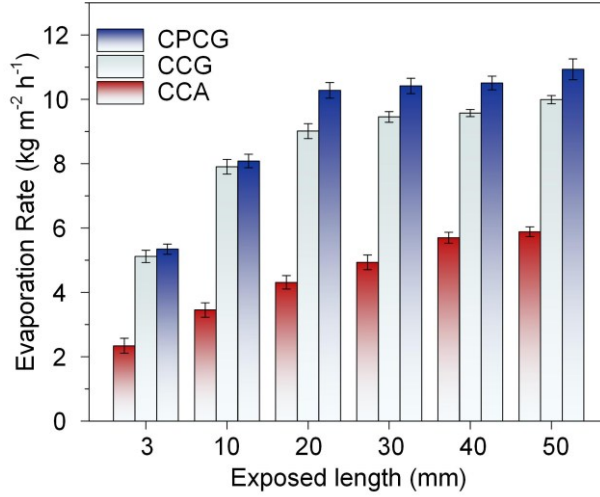


**Fig. S14** Solar evaporation rates of three cuboid chimneys at different exposed lengths.

### S9. Models and simulation results

In solar evaporation process, many physical effects must be considered, including fluid flow, heat transfer with phase change, and transport of participating water and gas, which were strongly coupled. In this study, the temperature distribution and gas flow on chimneys were simulated by a simplified mathematical model of multi-physic field, including laminar flow, moisture transport in the air and heat transfer in the moist air. In this model, the chimney was modelled as a porous medium, which was filled with water and vapor. The water and vapor phase were assumed to be in equilibrium inside this chimney. When evaporation happened, the vapor escaped from the chimney to the gas domain, and the varying water saturation extent was computed to model the heat and moisture transport by a two-phase flow with COMSOL Multiphysics.

The geometry, finite element mesh, and boundaries were shown in Fig. S15. There were two domains in this model, including the gas domain and the sample & water domain. The sample & water domain consisted of the exposed chimney and the bulk water. On the top of the chimney, a heat source boundary was set as  $Q_s = 3000 \text{ W}\cdot\text{m}^{-2}$  to simulate the solar energy input. Vapor was generated on the top and side surfaces of the chimney, and the surface of bulk water was set as moisture barrier (where the moisture transfer coefficient  $\beta$  equalled to 0) to avoid the evaporation of bulk water. Since the vapor escaped to atmosphere, the top and the side boundaries of the gas domain were set as the boundary of open flow, where the temperature equalled to the environment temperature ( $T = T_e$ ) and the relative humidity equalled to the environment humidity ( $\Phi = \Phi_e$ ). Water should be replenished by the diffusion on these side

and bottom boundaries of bulk water, where the temperature was set as  $T_e$  and the water molecular concentration was set as  $c_0$  ( $c_0$  was the concentration of water molecules in pure water,  $55555.6 \text{ mol/m}^3$ ). The chimney was illuminated by a static solar energy, and generated vapor expanded on the top and side surfaces in an initially quiescent surrounding gas. For the solar evaporator without gas channel, the process was assumed to have a symmetry at the middle line and the physical problems were thus computed in a symmetrical domain (Fig. S15a). For the solar evaporator with gas channel, since there was a size of 2 mm hole in the middle line, the symmetrical boundary cannot be added. Hence the process of the solar evaporator with gas channel was computed in the domain of Fig. S15b.

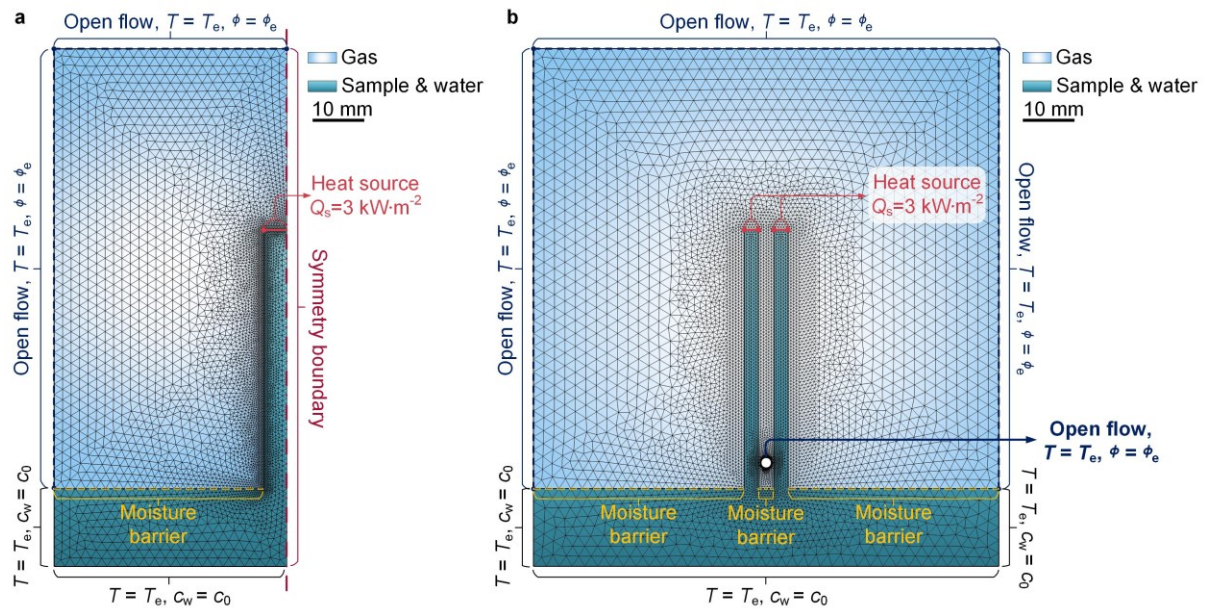


**Fig. S15** The geometry, finite element mesh, and boundaries of the solar evaporation model. (a) In the solar evaporator without gas channel. (b) In the solar evaporator with gas channel.

The fluid flow in the chimney is governed by a combination of the continuity equation and the momentum equation, which together form the Brinkman equations:

$$\frac{\partial \varepsilon_p \rho}{\partial t} + \nabla \cdot (\rho \vec{u}) = Q_m \quad (\text{SE } 2)$$

$$\frac{1}{\varepsilon_p} \rho \frac{\partial \vec{u}}{\partial t} + \frac{1}{\varepsilon_p} \rho (\vec{u} \cdot \nabla) \vec{u} - \frac{1}{\varepsilon_p} \nabla p = -\nabla p \mathbf{I} + \nabla \cdot \left\{ \frac{1}{\varepsilon_p} \left[ \mu (\nabla \vec{u} + (\nabla \vec{u})^T) - \frac{2}{3} \mu (\nabla \cdot \vec{u}) \mathbf{I} \right] \right\} - \left( \frac{\mu}{\kappa} + \frac{Q_m}{\varepsilon_p^2} \right) \vec{u} + \vec{F} \quad (\text{SE } 3)$$

where  $\mu$  is the dynamic viscosity,  $\vec{u}$  is the velocity field,  $\rho$  is the density of the fluid,  $p$  is the pressure,  $\varepsilon_p$  is the porosity,  $\kappa$  is the permeability of the porous medium, and  $Q_m$  is a mass source or sink. The influence of capillary driving force and gravity can be accounted for *via* the force term  $\vec{F}$ :

$$\vec{F} = -\frac{\vec{P}_c}{L} + \rho \vec{g} \quad (\text{SE 4})$$

where  $P_c$  is the capillary driving force (the minus sign in the governing equation indicates that its direction is opposite to the direction of gravity),  $L$  is the capillary length and  $g$  equals to gravity constant. The capillary driving force is introduced by the surface tension of a liquid on a meniscus in a capillary tube (Fig. S16). Since the capillary driving force depends on the solid-liquid-gas three-phase line and occurs on the gas-liquid interface, it is not necessary to consider the capillary driving force when the capillary is filled with liquid or gas only. Thus, when the water contact angle is 0, the capillary driving force can be calculated by:

$$P_c = \begin{cases} \frac{2\sigma}{R_c} & (s_1 > 0 \text{ and } \Phi < 0.58) \\ 0 & (s_1 = 0 \text{ or } \Phi \geq 0.58) \end{cases} \quad (\text{SE 5})$$

where  $\sigma$  is the surface tension coefficient,  $R_c$  is the radius of the capillary tube ( $R_c$  in this simulation is  $0.5 \mu\text{m}$ ), and  $s_1$  is the saturation index of water in the gas-liquid two phase flow.

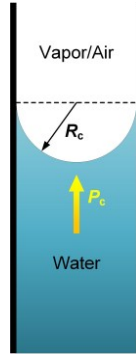


**Fig. S16** Schematic illustration of capillary driving force in the micro channel.

Besides  $s_1$ , in the gas-liquid two phase flow, the saturation index of gas ( $s_g$ ) should also be taken into consideration. These two saturation variables should fulfil the following constraint:

$$s_g + s_1 = 1 \quad (\text{SE 6})$$

In the porous domain, the velocity of the liquid phase ( $\vec{u}_l$ ) is small when it is compared to the velocity of the moist air ( $\vec{u}_g$ ), thus  $\vec{u}_l$  can be calculated by the gas phase pressure gradient ( $\nabla p_g$ ) and gravity:

$$\vec{u}_l = -\frac{\kappa_{r1}\kappa}{\mu_1} (\nabla p_g - \rho_l \vec{g}) \quad (\text{SE 7})$$

where  $\mu_1$  is the dynamic viscosity of the liquid phase and  $\rho_l$  is the density of the liquid phase.

The relative permeability coefficient of the liquid phase,  $\kappa_{r1}$  can be described by<sup>7</sup>:

$$\kappa_{rl} = \begin{cases} \left( \frac{s_l - s_{li}}{1 - s_{li}} \right)^3 & (s_l > s_{li}) \\ eps & (s_l \leq s_{li}) \end{cases} \quad (\text{SE 8})$$

where  $s_{li}$  is the irreducible liquid phase saturation index ( $s_{li}$  is 0.01 in this simulation), and  $eps$  is the floating-point relative accuracy (machine epsilon,  $2^{-52}$  or about  $2.2204 \times 10^{-16}$ , for double floating-point numbers).  $eps$  is included to ensure the relative permeability coefficient would always be positive.

In the free region, flow is described by the Navier-Stokes equation. However, in the porous region, the flow field of gas phase ( $\vec{u}_g$ ) can be calculated by the Brinkman equations (Equations SE 2 and SE 3)

The relative permeability coefficient of the gas phase,  $\kappa_{rg}$  can be described by<sup>7</sup>:

$$\kappa_{rg} = \begin{cases} 1 - 1.01s_l & (s_l < 1/1.01) \\ eps & (s_l \geq 1/1.01) \end{cases} \quad (\text{SE 9})$$

Based on the mass conservation equation for vapor and liquid water, the moisture transport can be described by the evolution of the total moisture content ( $W(\Phi)$ ):

$$\frac{\partial W(\Phi)}{\partial t} + \rho_g \vec{u}_g \cdot \nabla \omega_v + \nabla \cdot \vec{g}_w + \vec{u}_l \cdot \nabla \rho_l + \nabla \cdot \vec{g}_{lc} = 0 \quad (\text{SE 10})$$

$$W(\Phi) = \varepsilon_p s_l \rho_l + \varepsilon_p s_g \rho_g \omega_v \quad (\text{SE 11})$$

where the  $\rho_g$  is the density of the gas phase, the dimensionless parameter  $\omega_v$  is the vapor mass fraction in moist air, defined as:

$$\omega_v = \frac{M_v \Phi c_{sat}(T)}{\rho_g} \quad (\text{SE 12})$$

where  $M_v$  is the molar mass of the water vapor,  $c_{sat}$  is the vapor saturation concentration,  $T$  is the temperature.

The moisture diffusive flux ( $\vec{g}_w$ ) is defined as:

$$\vec{g}_w = -\rho_g D_{eff} \nabla \omega_v \quad (\text{SE 13})$$

where  $D_{eff}$  is the effective vapor diffusion coefficient in the porous medium. In the unsaturated medium, the  $D_{eff}$  can be calculated by Millington and Quirk equation:

$$D_{eff} = D_{va} \varepsilon_p^{\frac{4}{3}} S_g^{\frac{10}{3}} \quad (\text{SE 14})$$

where  $D_{va}$  is the vapor-air diffusivity.

The liquid water capillary flux ( $\vec{g}_{lc}$ ) can be defined from the capillary pressure gradient by a diffusion equation using the relative humidity:

$$\vec{g}_{lc} = -D_w \frac{\partial W(\Phi)}{\partial \Phi} \nabla \Phi \quad (\text{SE 15})$$

where  $D_w$  is the moisture diffusivity<sup>8</sup>:

$$D_w = 10^{-8} \times \exp\left(-2.8 + 2W(\Phi)/(\varepsilon_p \rho_s)\right) \quad (\text{SE 16})$$

where  $\rho_s$  is the solid phase density.

The moisture source ( $\overrightarrow{G_{\text{evap}}}$ ) induced by evaporation may be obtained from the transport equation for vapor:

$$\overrightarrow{G_{\text{evap}}} = \frac{\partial[\varepsilon_p \rho_g \omega_v (1-s_1)]}{\partial t} + \rho_g \overrightarrow{u_g} \cdot \nabla \omega_v + \nabla \cdot \overrightarrow{g_w} \quad (\text{SE 17})$$

In the heat transfer process, by making the local thermal equilibrium hypothesis for all phases (solid matrix, moist air and liquid water), the heat transfer equation can be described as:

$$(\rho C_p)_{\text{eff}} \frac{\partial T}{\partial t} + (\rho_g C_{p,g} \overrightarrow{u_g} + \rho_l C_{p,l} \overrightarrow{u_l}) \cdot \Delta T + \nabla \cdot \vec{q} = \overrightarrow{Q} + \overrightarrow{Q_{\text{evap}}} \quad (\text{SE 18})$$

$$\vec{q} = -k_{\text{eff}} \nabla T \quad (\text{SE 19})$$

where  $C_{p,g}$  and  $C_{p,l}$  are the moist air and liquid water heat capacities at constant pressure,  $\vec{q}$  is the conductive heat flux, and  $\overrightarrow{Q}$  is the source of heat.

The effective volumetric heat capacity at constant pressure  $(\rho C_p)_{\text{eff}}$  can be calculated as:

$$(\rho C_p)_{\text{eff}} = \theta_s \rho_s C_{p,s} + \varepsilon_p \left[ (1-s_1) \rho_g C_{p,g} + s_1 \rho_l C_{p,l} \right] \quad (\text{SE 20})$$

where  $\theta_s$  is the solid matrix volume fraction.

The effective thermal conductivity,  $k_{\text{eff}}$ , is calculated by:

$$k_{\text{eff}} = \theta_s k_s + \varepsilon_p \left[ (1-s_1) k_g + s_1 k_l \right] \quad (\text{SE 21})$$

where  $k_s$ ,  $k_g$  and  $k_l$  are the heat conductivity of the solid, the moist air and the liquid water, respectively.

The overall velocity ( $\overrightarrow{u_{\text{eff}}}$ ) can be expressed as the average of moist air and liquid water velocity:

$$(\rho C_p)_{\text{eff}} \overrightarrow{u_{\text{eff}}} = \rho_g C_{p,g} \overrightarrow{u_g} + \rho_l C_{p,l} \overrightarrow{u_l} \quad (\text{SE 22})$$

The heat sink due to water evaporation,  $\overrightarrow{Q_{\text{evap}}}$ , is defined as:

$$\overrightarrow{Q_{\text{evap}}} = L_v \overrightarrow{G_{\text{evap}}} \quad (\text{SE 23})$$

where  $L_v$  is the latent of the evaporation. In this study, we used the combination of Stationary Solver and Time-Dependent Solver in COMSOL Multiphysics for computing the solution, where the time step was 0 ~ 2000 s.

## **S10. Analysis of the simulation results**

The simulation results of the gas velocity, temperature in these samples, and relative humidity in the gas domain are shown in the Figs. 2b and 2c. These results show that the bottom-to-up channel plays a crucial role in enhancing evaporation rate by inducing directional airflows on both the inner and outer surfaces of the chimney, effectively eliminating eddies in the vapor layer. During the operation of a 3D solar evaporator, the upward movement of hot and humid air creates negative pressure at the evaporation front, drawing ambient air toward the evaporation surface and generating a chimney effect that enhances the utilization of environmental energy. Traditional solid 3D solar evaporator (represented by CPCG) engages ambient air only on their external surfaces, a phenomenon known as the external chimney effect. In contrast, the CPCGG not only facilitates a chimney effect on its external surface, but also introduces an internal chimney effect through a built-in bottom-to-up gas channel. We simulate the heat and mass transfer among the floating solar evaporator chimney, water vapor and the surrounding dry air, by using a multi-physics model. Laminar flow, moisture transport and heat transfer in the moist air are incorporated in the model (see Section S9, Figs. S15 and S16 in the Supplementary Information). Facilitated by the dual influence of the internal and external chimney effect, dry air from the surrounding environment is continuously pumped into the steam layer, flowing upward and carrying away evaporated water vapor from evaporator surface (Figs. 2b and S17a). Simultaneously, the directed airflow shears along the gas-liquid interface and brings kinetic energy into the evaporating interface. Consequently, solar evaporation rate is significantly enhanced through the directional airflow on both the inner and outer surfaces of the chimney with the bottom-to-up channel, which is further evidenced by the much higher evaporation rate of CPCGG as compared to CPCG.

For the sample lacking a bottom-to-up gas channel (CPCG), stagnant eddies current inevitably formed on the surface, creating a mass transport barrier in the water vapor layer (as illustrated in Figs. 2c and S17a). This meant that during the evaporation process of the traditional solid 3D solar evaporator (represented by CPCGG), eddies spontaneously formed within the steam layer. These vortices not only hindered the inflow of dry air and the outflow of moist air but also resulted in the evaporated water vapor returning to the evaporation surface through complex cyclonic paths.

When the exposed height of the floating solar evaporator chimney is merely 3 mm, the interaction between water vapor and dry air generates severe eddies at both top and sides of the solar evaporation front, with a cumulative eddy region thickness of approximately 14.7 mm.

The presence of a low-velocity humid air vortex shields the evaporation front and inhibits evaporation, then heat is transported to the bulk water through thermal conduction, resulting in inevitable heat loss. When the exposed length is 30 mm, which is higher than the height of the eddy region ( $\sim 11.8$  mm), although the height of the solar evaporation front surpasses the thickness of the eddy region, the velocity of self-driven airflow is insufficient to enable dry air to traverse the dense water vapor layer and reach the evaporation front effectively. In comparison, when exposed length further increases to 50 mm, dry air at the top of chimney penetrates the water vapor layer at a speed exceeding  $78 \text{ mm s}^{-1}$ , intensively facilitating evaporation that carries away a significant amount of heat. Nevertheless, some eddy regions with a thickness of approximately  $\sim 12.2$  mm persist at the bottom, and the inner structure which is not blown by airflow still cause dissipation of heat from the solar evaporation front to the bulk water.

These mechanisms of enhancing solar evaporation rate are further substantiated by the temperature distribution profile (Figs. 2d and 2e). In instances where there is no bottom-to-up gas channel in the floating solar evaporator chimney (CPCG), the temperature profiles along the middle line of chimney at different exposed lengths are shown in Fig. 2d. Along this middle line, the temperature at a height of 0 ( $T_0$ ) reflects the heat loss by diffusing from the evaporation front to the bulk water. As the exposed length increases from 3 mm to 50 mm,  $T_0$  decreases from  $31.7 \text{ }^\circ\text{C}$  to  $25.7 \text{ }^\circ\text{C}$ . Therefore, with the increase of the exposed length, the dry air that is pumped by the sucking effect of chimney facilitates the evaporation on the side surface by displacing moisture in the water vapor layer, which confines most of the heat near the evaporation front. Furthermore, the heat loss can be significantly reduced by the floating solar evaporator chimney with gas channel (CPCGG). We extract the temperature profiles along the inner line of this chimney with gas channel, as indicated by Fig. 2e. At the bottom of chimney, there exists a substantial region, approximately 21.5 mm in length, with temperature lower than the environment ( $< 25 \text{ }^\circ\text{C}$ ). This phenomenon is attributed to these regions being shielded from light illumination, and the presence of dry air flow within the gas channel facilitates the local evaporation rate, effectively enhancing evaporation and causing heat sink. Therefore, this chimney with bottom-to-up gas channel, which pumps dry air to foster the inner and outer evaporation, can realize thermal insulation between evaporation front and bulk water *via* negative ambient temperature barrier. This effectively reduces the heat loss and strengthens the gas flow on the side surface, thereby improving the overall evaporation rate.

The relative pressure induced by the chimney effect ( $P_{rc}$ ) can be calculated as following:

$$P_{rc} = P_{abs} - (P_{atm} - k_{atm} h_R) \quad (\text{SE } 24)$$

where  $P_{abs}$  is the absolute pressure of the gas,  $P_{atm}$  is the atmospheric pressure at the reference plane ( $P_{atm} = 101325 \text{ Pa}$ ),  $k_{atm}$  is the coefficient of atmosphere pressure decrease due to relative height under the action of gravity ( $k_{atm} = 11 \text{ Pa m}^{-1}$ ), and  $h_R$  is the relative height (Fig. S17b).

For the CPCGG, the relative pressure generated by the internal chimney effect was studied by the analysis line of  $AA'$  and showed in Fig. S17c. The result indicated that, the  $P_{rc}$  near the side hole (the inlet of the bottom-to-up gas channel) was  $-759 \text{ mPa}$ . The absolute value of  $P_{rc}$  increased with the relative height, and the peak value of  $P_{rc}$  near the outlet of the bottom-to-up gas channel was  $-788 \text{ mPa}$ . Therefore, the internal chimney effect generated a negative pressure relative to the environment, drawing external gas into the chimney internal gas channel through the side hole, with the suction effect intensified as the relative height increased. The relative pressure of the external chimney effect was further explored through analysis lines  $BB'$ ,  $CC'$ ,  $DD'$ ,  $EE'$  and  $FF'$ , as illustrated in Fig. S17d. Despite the increasing distance of these analysis lines from the side surface of CPCGG, the distribution of their  $P_{rc}$  at various relative heights was remarkably similar, and showed that the chimney effect was intensified with height. On the  $BB'$  line, situated  $1 \text{ mm}$  from the side surface of CPCGG, the  $P_{rc}$  near the bottom was about  $-755 \text{ mPa}$ , and near the top, it was around  $-787 \text{ mPa}$ . This indicates that negative pressure relative to the ambient pressure can also be generated on the external surface of the CPCGG, facilitating the extraction of dry air from the environment.

For the CPCG, the relative pressure of the external chimney effect was also examined using external vertical analysis lines. However, as the distance from these lines to the CPCG side surface increased, the distribution of the relative pressure ( $P_{rc}$ ) showed significant variation (Fig. S17e). Notably, within the relative height range of  $10 \text{ mm}$  to  $40 \text{ mm}$ , the absolute value of  $P_{rc}$  on the analysis line closest to the CPCG surface ( $BB'$ ) exhibited a downward trend compared to other analysis lines. This indicated the presence of a pressure gradient in the direction opposite to the gas flow between the  $BB'$  line and the  $FF'$  line. By analysing the pressure difference ( $\Delta P_{abs}$ ) between these lines of  $BB'$  and  $FF'$  with different relative heights, this counter-flow pressure difference, which opposes the chimney effect, was confirmed (as shown in Fig. S17f). For the CPCG, the maximum value of the pressure difference between these lines of  $BB'$  and  $FF'$  was about  $5.2 \text{ mPa}$ , which was  $478\%$  higher than that of the CPCGG ( $\sim 0.9 \text{ mPa}$ ). This pressure gradient in the CPCG could counteract the suction effect created by the chimney effect near the side surface of CPCG, leading to the formation of eddies or dead zones.

The uneven distribution of relative pressure ( $P_{rc}$ ) in the air environment adjacent to CPCG samples stemmed from the heating effect of the CPCG side surface on the surrounding air. Within the CPCG, heat diffused from the solar-heated top surface to the bulk water below through both the internal water and the material medium of CPCG. This diffusion persisted even when the exposed height was 50 mm, resulting in a temperature distribution along the midline of CPCG that remained above the ambient temperature (as shown in Figs. 2c and 2d). By examining the temperature distribution across five horizontal analysis lines at different relative heights (including  $MM'$ ,  $NN'$ ,  $OO'$ ,  $PP'$ , and  $QQ'$ ), it suggested that the heat conducted along the midline inside the CPCG also transferred into the environment through the side surface of CPCG, thereby heating the air and vapor (Fig. S17g). Consequently, in traditional solid 3D solar evaporators (represented by the CPCG), the heat emanating from their sides heated the air and vapor along the sidewall. This heating action forced the heated air to press against the ambient air directed towards the sidewall, creating a high-temperature and high-pressure vapor barrier along the side surface of CPCG. This barrier, in turn, generated eddy currents on the side, or flow dead zones, obstructing both the escape of vapor and the influx of ambient energy. Therefore, simulation results revealed that traditional solid 3D solar evaporators (represented by CPCG) face two critical challenges: internally, heat was transferred downwards to the bulk water through the medium inside the evaporator, resulting in thermal energy losses (Fig. 2d); externally, heat emanating from the sidewalls heated the surrounding air (Fig. S17g) and generates eddies or flow dead zones (Figs. 2c and S17a), further restricting the evaporation.

In contrast, for a CPCGG equipped with a bottom-up gas channel, the low temperature effect on its sidewall led to a modest pressure increase (between the  $BB'$  and  $FF'$  lines) of merely 0.9 mPa (Fig. S17f), which was just 17% of that observed in a traditional solid 3D solar evaporator (CPCG). This tiny amount of reverse pressure generated near the side surface of the CPCGG was unable to counteract the large amount of kinetic energy carried by the ambient air during its flow, thus cannot completely reverse the direction of the ambient air flow, perfectly eliminating eddies and flow dead zones. Fig. S17h showed the humidity distribution along five horizontal test lines at different relative heights (including  $MM'$ ,  $NN'$ ,  $OO'$ ,  $PP'$ , and  $QQ'$ ). When a relative humidity of 0.5 was considered to be the boundary of the vapor layer, it exhibited that the maximum width of the vapor layer for CPCGG was ~8.0 mm on the  $MM'$  line, which represented a 30% reduction compared to that of CPCG. This reduction was attributed to elimination of eddies or flow dead zones in the air by CPCGG. Further analysis of the flow

velocity distribution on these  $MM'$  and  $NN'$  lines revealed that CPCGG exhibited higher flow velocities in the air environment near the side surface of the sample. Consequently, CPCGG enhanced the nearby vapor flow by eliminating eddies in the side air environment, thereby improving the absorption and utilization of ambient energy and facilitating the evaporation process.

In conclusion, simulation analysis in this study uncovers two pivotal methods to boost the performance of 3D solar evaporators: firstly, by restricting internal heat diffusion, and secondly, by eliminating external eddies or flow dead zones. Drawing on these insights, the research introduces a novel design of a 3D solar evaporator with a bottom-to-up gas channel (CPCGG), marking a significant advancement over the traditional solid 3D solar evaporator (CPCG). The innovation at the heart of this design features a vertical gas channel running from the bottom to the top of the 3D evaporator, with strategically placed small holes near the base to ensure connectivity with the external atmosphere. This design aims to leverage the chimney effect that activates both internally and externally, where the suction induced by the internal channel draws in dry air from the environment and facilitates the removal of internal heat, effectively eliminating external eddies or flow dead zones. Consequently, dry air directly reaches the vapor layer along the flow lines without interference from eddies, while moist air is efficiently vented to the atmosphere. This significantly improves the exchange efficiency between vapor and dry air, and prevents the recirculation of vapor onto the evaporation surface. The CPCGG also generates a substantial region ( $\sim 21.5$  mm in length) with a temperature lower ( $< 25$  °C) than the surrounding environment (Fig. 2e). All of these significantly improves the ability of CPCGG to harvest energy from the environment.

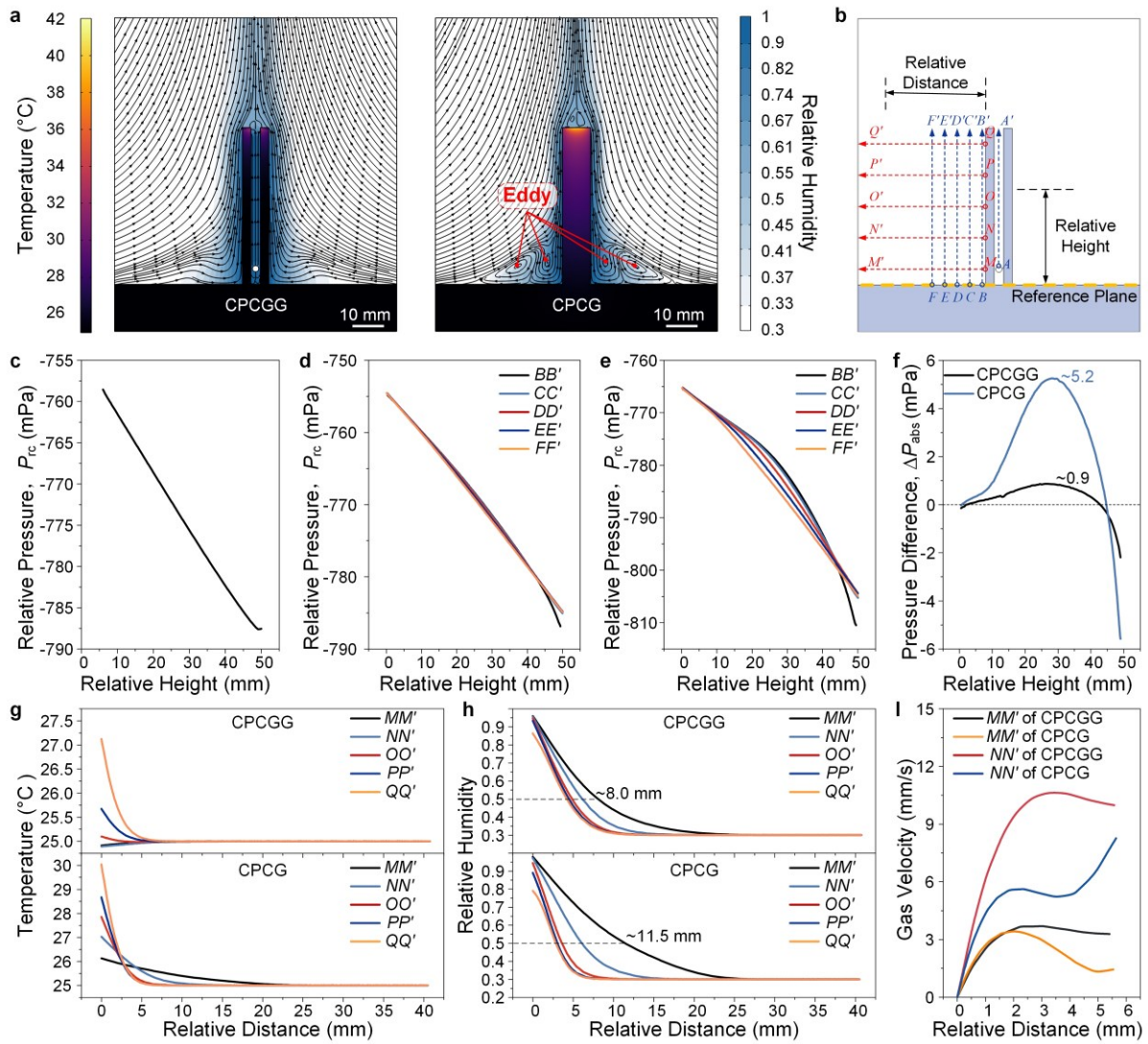


**Fig. S17** Simulation results of CPCGG and CPG, where the exposed height is 50 mm. (a) The distribution of gas streamline, temperature, and relative humidity on the simulation results of CPCGG and CPG. (b) Schematic diagram of these analysis lines. For the CPCGG, the line of  $AA'$  is the internal line in the gas channel, which starts from the side hole to the top of the CPCGG. For the CPCGG and CPG, these lines of  $BB'$ ,  $CC'$ ,  $DD'$ ,  $EE'$  and  $FF'$  are the external lines of the sample in the gas domain, which are vertical and start from the reference plane to the height near the top of sample. The spacing between these lines is 5 mm, and the distance between the line of  $BB'$  and the side surface of the sample is 1 mm. For the CPCGG and CPG, these lines of  $MM'$ ,  $NN'$ ,  $OO'$ ,  $PP'$  and  $QQ'$  are the external lines of the sample in the gas domain, which are horizontal and start from the side surface of the sample to the far-field ambient. The spacing between these lines is 10 mm, and the distance between the line of  $MM'$  and the reference plane is 5 mm. (c) The relative pressure of CPCGG internal gas channel in the line of  $AA'$  with different relative height generated by the internal chimney effect. The relative

pressure of d) CPCGG and e) CPCG external ambient in these lines of  $BB'$ ,  $CC'$ ,  $DD'$ ,  $EE'$  and  $FF'$  induced by the external chimney effect. (f) The pressure difference between the line of  $BB'$  and  $FF'$  of CPCGG and CPCG with different relative height. (g) The temperature and (h) humidity distribution in these lines of  $MM'$ ,  $NN'$ ,  $OO'$ ,  $PP'$  and  $QQ'$  of CPCGG and CPCG with different relative distance. (i) The comparison of gas velocity distribution near the side surface of CPCGG and CPCG.

### **S11. The schlieren image of vapor**

To experimentally validate the chimney effect, we employed the single-mirror off-axis schlieren system (Fig. S18a), which uses a knife edge as a half-plane spatial mask to filter the spatial spectrum of light beams passing through the flow field. This setup visualizes variations in air refractive index caused by vapor flow, thereby revealing gas movement around the structure.<sup>9</sup> The principle involves a light beam emitted from a point source, reflected by a concave mirror, and focused to form an image captured by a camera. The area in front of the concave mirror contains a non-uniform flow field. When the refractive index of the gas in this region changes, the light path is affected, causing some of the light to be blocked by the knife edge and unable to reach the camera, thus generating a ripple image with alternating light and dark. According to the working principle of the single-mirror off-axis schlieren system, the essential components include a concave mirror, a knife edge, a point light source, and a camera. The point light source is positioned at a distance equal to twice the focal length of the concave mirror. Then, the mirror reflects and focuses the light to form an image, and the knife edge is placed at the focal point to obstruct half of the light spot. The camera (AcutEye, Rocketech Technology Co., Ltd, China) is adjusted to ensure a clear, high-contrast field of view (Fig. S18a). In this study, the spherical concave mirror used has a diameter of 203 mm and a focal length of 750 mm.

The schlieren imaging results confirm the presence of directional vapor flow of CPCGG, driven by the chimney effect, which enables spontaneous vapor flow regulation and minimizes boundary layer thickness (Fig. S18b). In contrast, the CPCG exhibits a noticeably thicker boundary layer due to side eddies disrupting vapor removal (Fig. S18c). These experimental observations corroborate our simulation findings and provide direct visual evidence of the chimney effect.

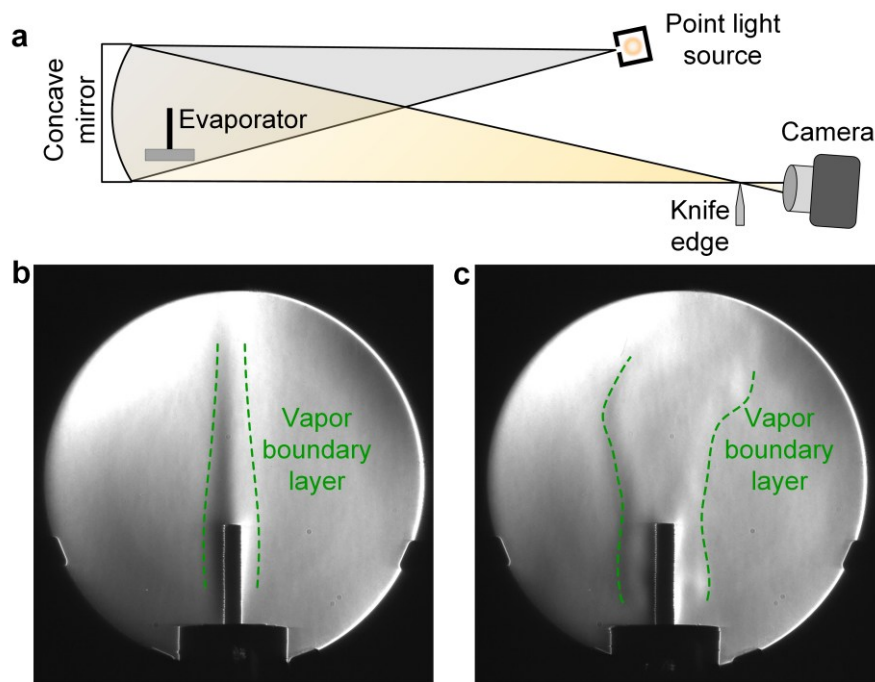


**Fig. S18** Experimental visualization of the chimney effect using the schlieren method. (a) Schematic illustration of the single-mirror off-axis schlieren system used for flow field visualization. Schlieren photographs of (b) CPCGG and (c) CPCG after 1 hour of exposure under 3-Sun illumination. The CPCGG shows clear directional vapor flow, and the CPCG shows a thicker boundary layer.

## S12. The results of infrared photography

The temperature distribution of the CPCGG under 3-Sun illumination was monitored using an infrared camera. Infrared imaging results indicate that the top surface temperature of the CPCGG is the highest and stabilizes quickly, maintaining a range between 36.3 °C and 37.3 °C (as shown in Fig. S19a). Side-view infrared photography reveals that when the temperature at the top of the CPCGG stabilizes, the temperature distribution in vertical direction also remains stable (Fig. S19b). During the operation of the 3D solar evaporator, the upward movement of hot and humid air generates negative pressure at the evaporation front. This negative pressure draws ambient air toward the evaporation surface, thereby creating a chimney effect, which enhances the utilization of environmental energy. The stability of the temperature distribution reflects the stability of the negative pressure and the chimney effect.

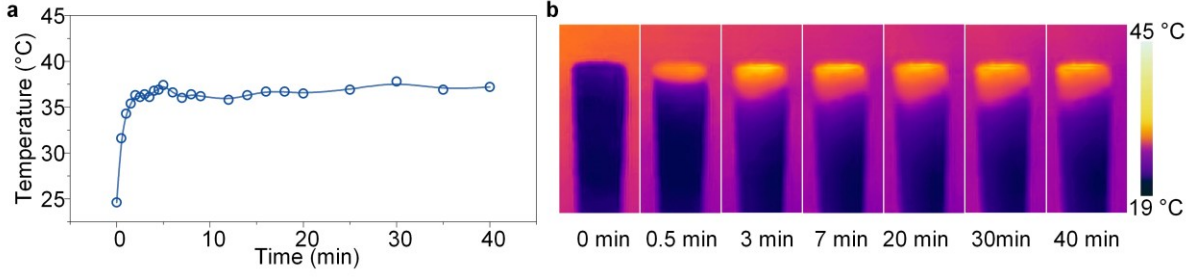


**Fig. S19** Surface temperatures of the CPCGG under 3-Sun illumination. (a) The maximum temperature on the top surface with different time. (b) Images of temperature distribution recorded by infrared camera with different time.

### S13. Design of the gas channel size, the side hole size and the side hole position.

The capillary pressure produced by the bending of the water surface in the gas channel can be calculated using the following equation:

$$P_{gc} = \frac{\sigma}{r_{g1}} + \frac{\sigma}{r_{g2}} \quad (\text{SE 25})$$

where  $r_{g1}$  and  $r_{g2}$  represent the two different principal curvature radii of the liquid film surface in the gas channel. When perforated holes are present on the side of the gas channel, the curvature of the water film in the direction of the side hole is not constrained by the inner diameter of the gas channel. In this case, the capillary pressure calculation only considers the contribution of the radius of curvature of the water film in the plane perpendicular to the side hole. When the water contact angle is  $0^\circ$ , this curvature radius is equal to the radius of the gas channel ( $r_{gc}$ ). Thus, the capillary pressure in a gas channel with side hole can be calculated as:

$$P_{gc} = \frac{\sigma}{r_{gc}} \quad (\text{SE 26})$$

Therefore, the height at which the water film can overcome gravity under the action of capillary in the gas channel can be calculated as:

$$h_{gc} = \frac{\sigma}{r_{gc} \rho_w g} \quad (\text{SE 27})$$

The relationship between  $h_{gc}$  and  $r_{gc}$  is showed in Fig. S20, where  $\sigma$  is  $72.1 \text{ mN m}^{-1}$ ,  $\rho_w$  is  $1000 \text{ kg m}^{-3}$  and  $g$  is  $9.8 \text{ N kg}^{-1}$ . The Fig. S20 exhibits that when  $R_{gc}$  is reduced to  $0.1 \text{ mm}$ ,  $h_{gc}$  rapidly increases to  $73.6 \text{ mm}$ . Therefore, to prevent the water film in the gas channel from blocking airflow,  $h_{gc}$  must be less than  $5 \text{ mm}$ , and the corresponding  $r_{gc}$  needs to be greater than  $1.47 \text{ mm}$ . Based on this, the gas channel size designed in this study is  $3 \text{ mm}$ , with  $r_{gc}=1.5 \text{ mm}$ , which meets the design requirements.

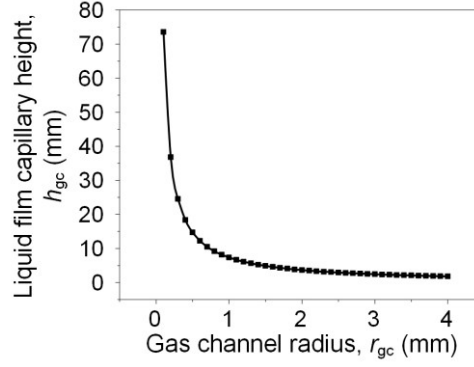


**Fig. S20** The relationship between the capillary height of liquid film in gas channel and the radius of gas channel.

According to the simulation results, the evaporation rate of one sample ( $R_s$ ) can be calculated by the following formula:

$$R_s = R_{Ts} + R_{Es} + R_{Is} \quad (\text{SE 28})$$

where  $R_{Ts}$ ,  $R_{Es}$  and  $R_{Is}$  represent the evaporation rates of a single sample on the top surface, external surface and internal surface, respectively (Figs. S21a and S21b). The  $R_{Ts}$ ,  $R_{Es}$  and  $R_{Is}$  can be calculated using the following formulas:

$$R_{Ts} = \int_{r_i}^{r_e} 2\pi r F_{Tw}(r) dr \quad (\text{SE 29})$$

$$R_{Es} = \int_0^H 2\pi r_e F_{Ew}(h) dh \quad (\text{SE 30})$$

$$R_{Is} = \int_0^H 2\pi r_i F_{Iw}(h) dh \quad (\text{SE 31})$$

where  $r_e$  and  $r_i$  are the external and internal surface radius of the chimney structure, respectively.  $H$  represents the height of the sample.  $F_{Tw}(r)$ ,  $F_{Ew}(h)$  and  $F_{Iw}(h)$  represent the water vapor flux at different locations of the top surface, external surface and internal surface on the sample, respectively. These values are obtained from COMSOL Multiphysics software.

The water supply rate at different height ( $l_h$ ) can be calculated using the following formulas:

$$SR_w(l_h) = \int_{r_i}^{r_e} \frac{2r F_{Tw}(r) dr}{(r_e^2 - r_i^2) \rho_w} + \int_{l_h}^H \frac{2r_e F_{Ew}(h) dh}{(r_e^2 - r_i^2) \rho_w} + \int_{l_h}^H \frac{2r_i F_{Iw}(h) dh}{(r_e^2 - r_i^2) \rho_w} \quad (\text{SE 32})$$

The simulation results show that increasing the gas channel diameter enhances gas flow velocity (Fig. S21c) but reduces the water supply rate (Fig. S21d), ultimately lowering the overall evaporation rate (Fig. S21e). This is attributed to the thinner sidewalls in larger channels, which increase flow resistance for liquid transport. Based on this trade-off, the gas channel diameter is determined to be 3 mm.

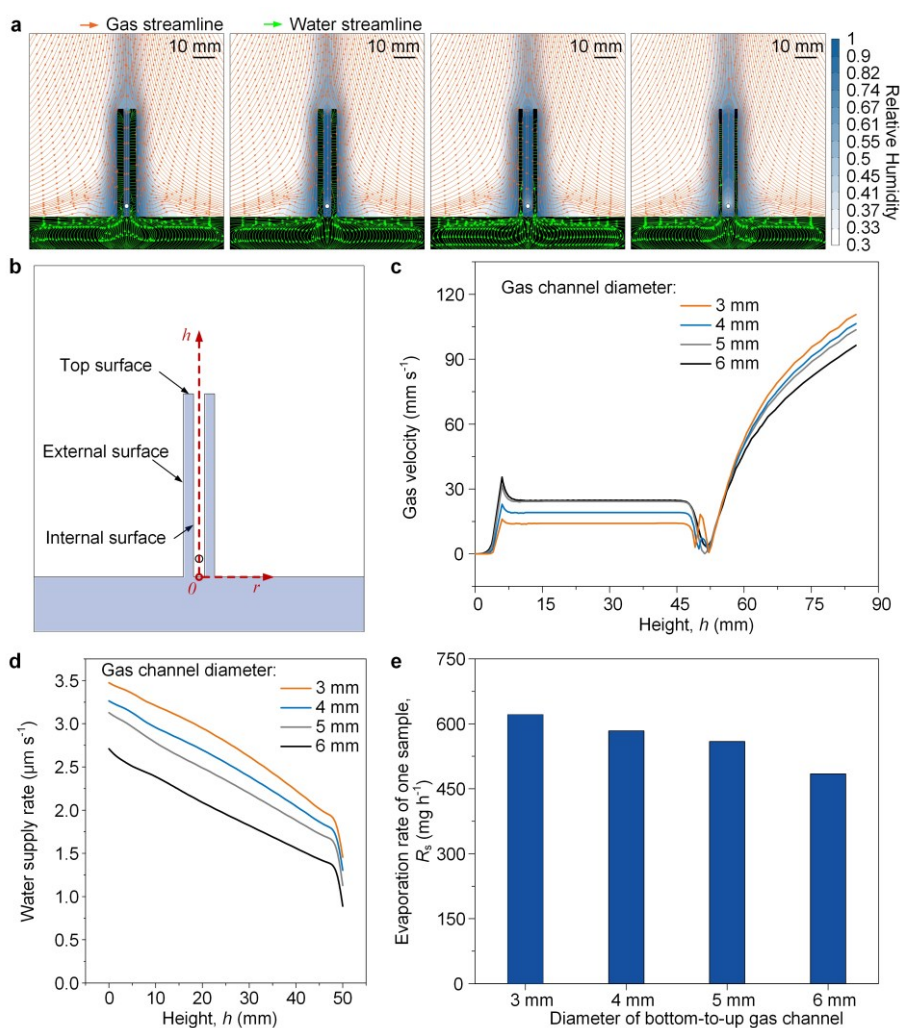


**Fig. S21** Effect of gas channel diameter on flow dynamics and evaporation rate under 3-Sun illumination. (a) Gas and water streamlines for channels with diameters of 3, 4, 5, and 6 mm. (b) Illustration of the sample coordinate system in simulation results. (c) Gas velocity profile along the centerline of the gas channel. (d) Water supply rates for different channel diameters. (e) Evaporation rates for one sample with varying channel diameters.

The effects of side hole position on flow characteristics and evaporation were analysed by testing side hole heights of 5, 15, 25, and 35 mm from the base (Fig. S22). The results reveal that vapor removal is primarily effective in the region above the side hole, while the region below shows negligible gas flow (Figs. S22a and S22b). Although the side hole height had little effect on water supply (Fig. S22c), it did influence local evaporation (Fig. S22d). The simulations showed a small peak in evaporation 0.8~1 mm above the side hole, caused by upward convection of dry air (Fig. S22d). As the side hole height increased, the total evaporation rate gradually decreased (Fig. S22e). Thus, the side hole height in our design was 5 mm.

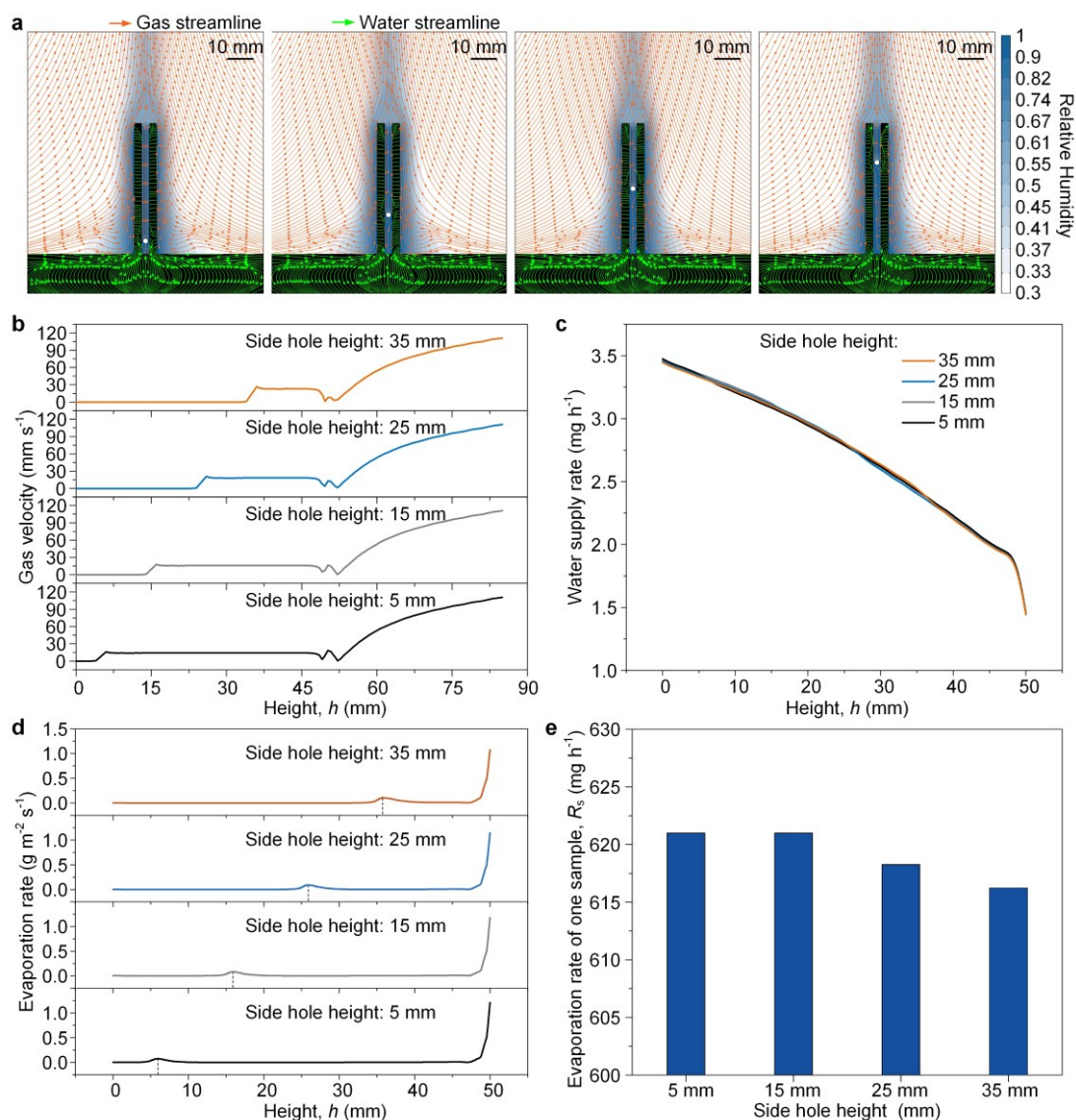


**Fig. S22** Effect of side hole position on flow characteristics and evaporation under 3-Sun illumination. (a) Gas and water streamlines for side hole positions at 5, 15, 25, and 35 mm. (b) Centerline gas velocity profiles for different side hole heights. (c) Water supply rate comparison for each configuration. (d) Local evaporation rate along the internal surface at various hole positions. (e) Total evaporation rate as a function of side hole height. The side hole diameter is 2 mm.

The effects of side hole position on flow characteristics and evaporation were analysed by testing side hole diameters of 0, 0.5, 1, and 2 mm (Fig. S23). When the side holes were sealed (0 mm), gas flow velocity in the channel was negligible. Increasing the side hole size to 2 mm raised the gas flow velocity to approximately 14 mm s<sup>-1</sup> (Figs. S23a and S23b). However, the side hole size had minimal impact on water supply (Fig. S23c). The enhanced gas flow primarily promoted vapor removal *via* the chimney effect. The simulation also showed that the

relative improvement in evaporation rate on the internal surface ( $R_{Is}$ ) increased significantly from 0 to 1 mm but plateaued beyond 1 mm, suggesting that the dry air intake reaches saturation above this threshold (Figs. S23d and S23e).

In the manufacturing process, due to 3D printing accuracy limitations and the shrinkage caused by post-processing, the final size of the side hole is approximately 1.6 mm, which is sufficient to allow the side hole to fully draw in dry air.

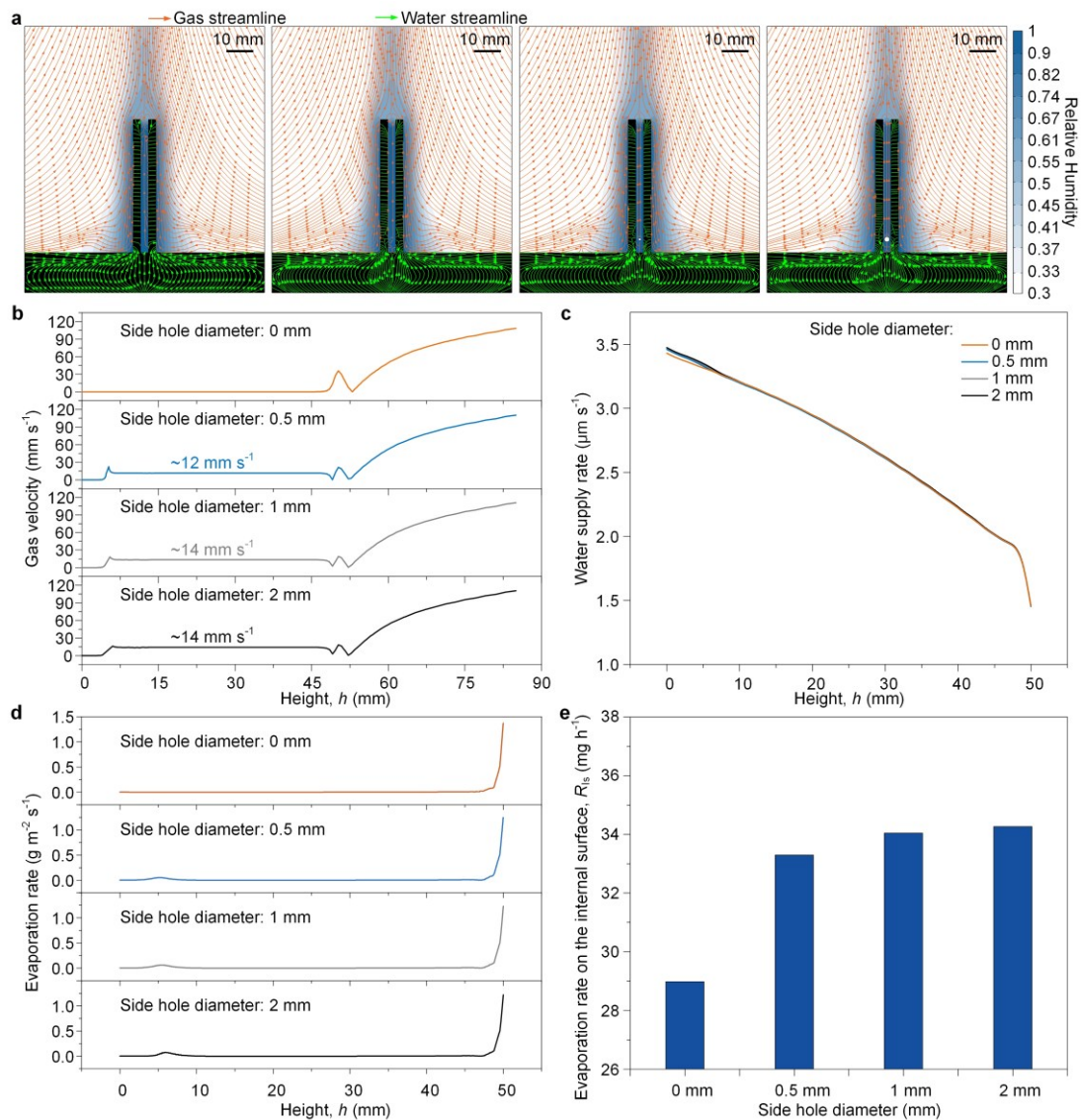


**Fig. S23** Effect of side hole size on flow behavior and evaporation under 3-Sun illumination. (a) Gas and water streamlines for side hole diameters of 0, 0.5, 1, and 2 mm. (b) Gas velocity profiles along the channel centerline. (c) Water supply rates as a function of side hole diameter. (d) Local evaporation rates on the internal surface for different side hole sizes. (e) Evaporation rate on the internal surface  $R_{Is}$  for different side hole diameters. The side hole position is 5 mm.

#### S14. Transmittance spectrum

The transmittance spectrum of CA-GO and porous CA-GO with the thickness of 5 mm are shown in Fig. S24. The average transmittance of CA-GO and porous CA-GO is 0.013% and 0.023%, respectively (Fig. S24). Considering that the thickness of the sample is more than 8.5 mm even when the incident sunlight is tilted and the average reflectance is 3.362% (~3.4%) of porous CA-GO, the average solar spectral absorption of porous CA-GO is ~96.6%.

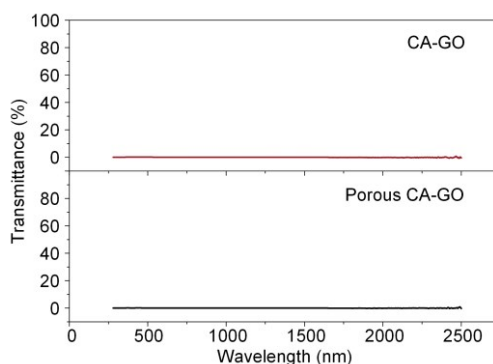


**Fig. S24** Transmittance spectrum of bulk and porous CA-GO samples after being soaked in deionized water for three days.

#### S15. Vapor generation under dark conditions and analysis of energy utilization efficiency

When the ambient vapor is not saturated, evaporation can proceed even without a temperature difference between the evaporator and the surrounding air, due to a non-zero concentration gradient. This process, known as dark evaporation or evaporation that harvests ambient energy, contributes to overall vapor production despite the absence of solar flux. The dark evaporation of different evaporators was tested in a dark box at an ambient temperature of 25 °C. All experiments were repeated three times, and the average values were calculated. The dark evaporation of CPCG demonstrated that as the exposed height of the 3D evaporator increased, the rate of dark evaporation consistently increased (Fig. S25a), benefiting from the enlarged contact area with the ambient dry air and thereby harvesting more ambient energy.

For the CCA, the CCG, and the CPCG, when their exposed height is < 1 mm, it reflects the dark evaporation rate of water in the printed CA, printed CA-GO and printed porous CA-GO materials (Fig. S25b). The equivalent evaporation enthalpy ( $E_{\text{equ}}$ ) of water in these materials can be estimated using a methodology proposed in previous studies.<sup>10, 11</sup> This involves comparing the evaporation rates of the solar evaporator and bulk water under identical dark conditions and assuming equal environmental power input for both scenarios, which has

$$E_{\text{equ}} = E_0 \frac{m_0}{m_g} \quad (\text{SE 33})$$

where  $E_0$  and  $m_0$  are the vaporization enthalpy and mass change of bulk water, respectively, and  $m_g$  is the mass change on these 2D evaporation surface of the printed CA, printed CA-GO or printed porous CA-GO materials. The evaporation enthalpy of bulk water is  $2.26 \text{ kJ g}^{-1}$ . The equivalent water evaporation enthalpy of the printed CA, the printed CA-GO and the printed porous CA-GO were  $1.14 \text{ kJ g}^{-1}$ ,  $1.06 \text{ kJ g}^{-1}$  and  $1.12 \text{ kJ g}^{-1}$ , respectively (Fig. S25c).

The energy utilization efficiency ( $\eta$ ) of solar evaporators can be calculated as:

$$\eta = \frac{\dot{m}E_{\text{equ}}}{P_{\text{solar}}} \quad (\text{SE 34})$$

where the  $P_{\text{solar}}$  is the solar irradiation power.

The energy utilization efficiencies of CCA, CCG and CPCG with different exposed height under 3-Sun are provided to investigate the contribution of exposed height for enhanced evaporation. Fig. S25d presents the energy utilization efficiency of CCA, CCG, and CPCG at varying exposed heights under 3-Sun illumination. For CPCG, an increase in exposed height to 50 mm elevates the solar energy utilization efficiency to 113.8%, exceeding the limit of traditional 2D solar evaporators. At an exposed height of 3 mm, the energy efficiency of CPCG stands at 55.6%. Consequently, for CPCG, elevating the exposed height to 50 mm resulted in more than 58.2% of the energy harvests from the ambient contributing to water evaporation. For CCG and CCA samples, the energy efficiencies at an exposed height of 50 mm reach 97.9% and 62.1%, respectively. Considering the energy utilization efficiency at 3 mm being 50.2% for CCG and 24.7% for CCA, elevating the exposed height to 50 mm results in more than 47.7% and 37.4% of the energy harvested from the ambient contributing to water evaporation for CCG and CCA, respectively. Moreover, the marginal 0.7% higher solar absorption rate of porous CA-GO over CA-GO in water suggests that the superior performance of CPCG in solar energy utilization and ambient energy harvesting, comparing to CCG, is mainly due to the porous CA-GO material, which decreases thermal resistance by directly feeding water to the photo-thermal interface and reduces thermal radiation loss by internal reflection at the same interface.

Fig. S25e shows the dark evaporation rates of CPCG and CPCGG at an exposure height of 50 mm, with rates of  $1.61 \text{ kg m}^{-2} \text{ h}^{-1}$  and  $2.58 \text{ kg m}^{-2} \text{ h}^{-1}$ , respectively. This demonstrates that, in a dark environment, the energy utilization efficiency of CPCGG in harvesting ambient energy is 60% greater than that of CPCG. These rates significantly exceed the dark evaporation rate of pure bulk water and that of water in printed porous CA-GO (Figs. S25b and S25e). Such results reveal that CPCGG leverages ambient energy for dark evaporation not just *via* its

external surface but also through the internal surfaces of its integrated gas channels, markedly boosting its capacity to utilize ambient energy and enhancing the dark evaporation rate. Consequently, under 3-Sun conditions, the energy utilization efficiency of CPCGG increases to 154%, representing a 35% improvement over CPCG (Fig. S25f). It should be noted that the side hole play a role in promoting the evaporation process of CPCGG. If the side holes are blocked, the solar energy utilization rate of CPCGG is reduced to 148%, and the evaporation rate under 3-Sun conditions is reduced to  $14.2 \text{ kg m}^{-2} \text{ h}^{-1}$ . This means that blocking the side hole prevents the flow of outside dry air into the bottom-up gas channel inside the CPCGG, thus preventing the CPCGG from harvesting environmental energy (Fig. S25f).

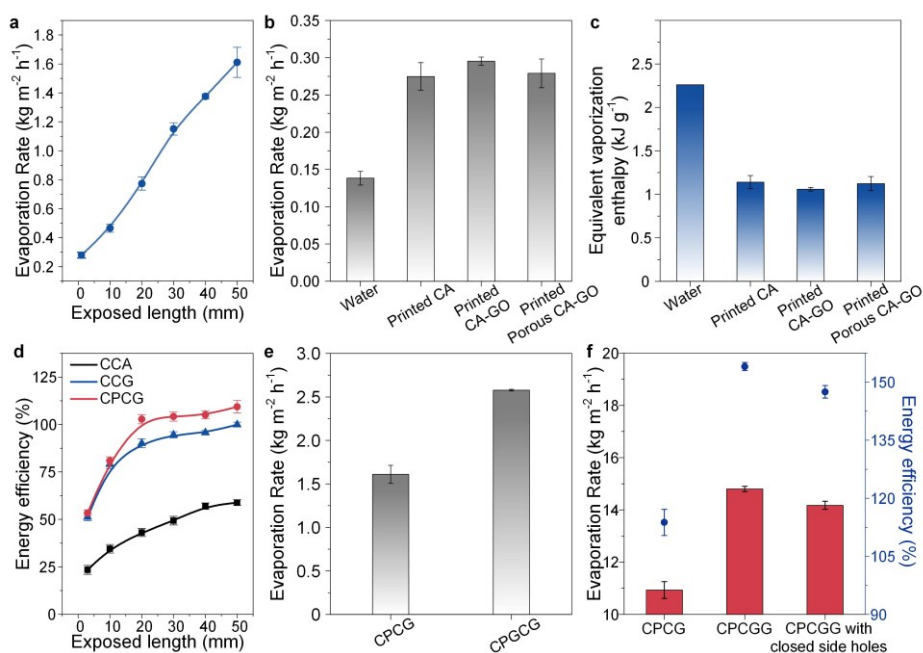


**Fig. S25** Dark evaporation and analysis of energy utilization efficiency. (a) The evaporation rate of CPCG with different exposed heights in the dark condition. (b) The comparison of dark evaporation rate and (c) equivalent water vaporization enthalpy of bulk water, and water in printed CA, printed CA-GO and printed porous CA-GO. (d) Energy utilization efficiency of CCA, CCG and CPCG with different exposed heights under 3-Sun illumination. (e) The evaporation rate of CPCG and CPCGG with the exposed height of 50 mm in the dark condition. (f) The evaporation rate and energy utilization efficiency of CPCG, CPCGG, and CPCGG with the closed side hole, where the exposed height is 50 mm and the sunlight illumination is 3-Sun. Three experiments were conducted and the average value was calculated as water evaporation rate and efficiency.

## S16. Effect of sunlight incidence angles, $\theta$

Unlike conventional 2D solar evaporators, 3D structures can absorb solar flux through the side surface when the sunlight incidence is tilted (Fig. S26a). This explains the better energy utilization capacity of 3D evaporators. Sunlight incidence angle was adjusted by changing the position and angle of inclination of solar simulator. The distance between the aluminium foil and the surface of bulk water was 3~5 mm to prevent the bulk water from being heated by aluminium foil (Fig. S26b).

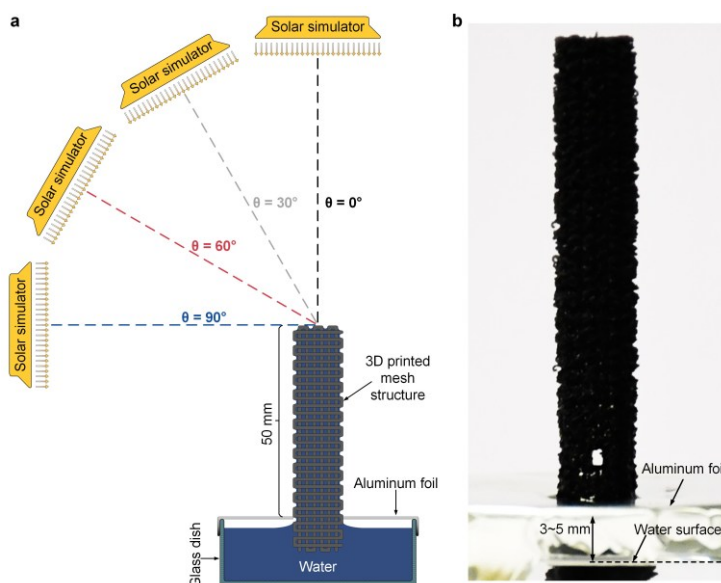


**Fig. S26** Solar evaporation with different sunlight incidence angle under 1-Sun illumination. (a) Schematic diagram of the sunlight incidence angle. (b) A digital photograph illustrating the position relationship between the surface of bulk water and aluminium foil.

## S17. Analysis of energy utilization efficiency under simulated natural sunlight illumination (1-Sun)

The solar evaporation rate under simulated natural sunlight (1-Sun) was determined with an incident angle of  $0^\circ$  (as detailed in Section S16 and illustrated in Fig. S26a). At an exposed height of  $< 1$  mm, the solar evaporation rates for CCA, CCG, and CPCG are found to be  $0.9 \text{ kg m}^{-2} \text{ h}^{-1}$ ,  $1.3 \text{ kg m}^{-2} \text{ h}^{-1}$ , and  $1.4 \text{ kg m}^{-2} \text{ h}^{-1}$ , respectively, with corresponding energy utilization efficiencies of 28%, 38%, and 44% (Fig. S27a). When the exposed height is increased to 50 mm, the energy utilization efficiencies for CCA, CCG, and CPCG rise dramatically to 136%, 173%, and 203% (Fig. S27b), respectively. This indicates that elevating the sample height facilitates the extraction of additional energy from the environment.

When the exposed height of CPCGG is 50 mm, the solar evaporation rates for CPCGG are found to be  $10.2 \text{ kg m}^{-2} \text{ h}^{-1}$  (Figs. 3a and S27b), which are lower than their performances under 3-Sun illumination (Fig. 2a). However, the 3-Sun lighting condition simulates a highly concentrated light field typical of a condenser environment, which usually produces a small diameter spotlight (30 mm in this study, Section S6 and Fig. S12), thus posing challenges in heating the surrounding ambient. In contrast, natural sunlight conditions differ as they can heat the surrounding ambient air when the sunlight is not focused. This is particularly effective in the evaporation process where water molecules in the air strongly absorb solar radiation in the infrared spectrum at wavelengths of  $2.66 \text{ }\mu\text{m}$ ,  $2.73 \text{ }\mu\text{m}$ , and  $6.27 \text{ }\mu\text{m}$ ,<sup>12</sup> thereby further enhancing the energy available from the environment. Therefore, under natural sunlight illumination, the contribution of ambient energy to the evaporation process is significantly increased, especially under the chimney effect where ambient energy is continuously supplied to the gas-liquid evaporation interface. This effect enables the CPCGG to utilize energy up to 317% relative to the solar radiation directly received by itself (Fig. S27b). Moreover, water transportation to the top is crucial for 3D evaporators. Under 3-Sun illumination, water evaporation rate is too fast so that water supplementation might be the rate-limiting step hindering high evaporation rate. In contrast, water transport under 1-sun illumination is adequate, and evaporation would not be restricted by insufficient water supply. This also explains why evaporation rate under 3 sun is not significantly higher the rate under 1-sun.

To verify that the chimney effect and thermal localization remain significant under practical 1-Sun conditions, a comprehensive analysis was conducted (Fig. S28), including simulation, schlieren imaging, infrared thermal imaging, total evaporation rate, apparent energy utilization efficiency, cold evaporation rate, and the proportion of cold evaporation at different exposed lengths. Both the simulation and schlieren imaging confirm that the chimney effect remains active under 1-Sun illumination, facilitating directional vapor flow within the CPCGG structure (Figs. S28a and S28b). Infrared thermal images further demonstrate that heat is effectively confined to the top region of CPCGG, indicating strong thermal localization (Fig. S28c). Performance measurements under 1-Sun conditions show that CPCGG enhances both the total evaporation rate and the apparent energy utilization efficiency compared to control samples (Fig. S27b). Additionally, cold evaporation measurements reveal that its contribution remains below 25.5% (Figs. S28d and S28e), confirming that the dominant evaporation mechanism is photothermal-driven, enhanced by both the chimney effect and localized heating. These results

collectively demonstrate that both the chimney effect and thermal localization play critical roles in maintaining high performance under practical 1-Sun conditions.

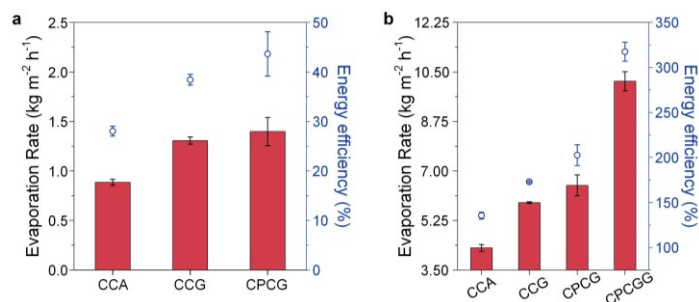


**Fig. S27** Solar evaporation rate and energy utilization efficiency of different sample under the simulated natural sunlight illumination. (a) The exposed height is < 1 mm. (b) The exposed height is 50 mm. Three experiments were conducted and the average value was calculated as water evaporation rate and efficiency.

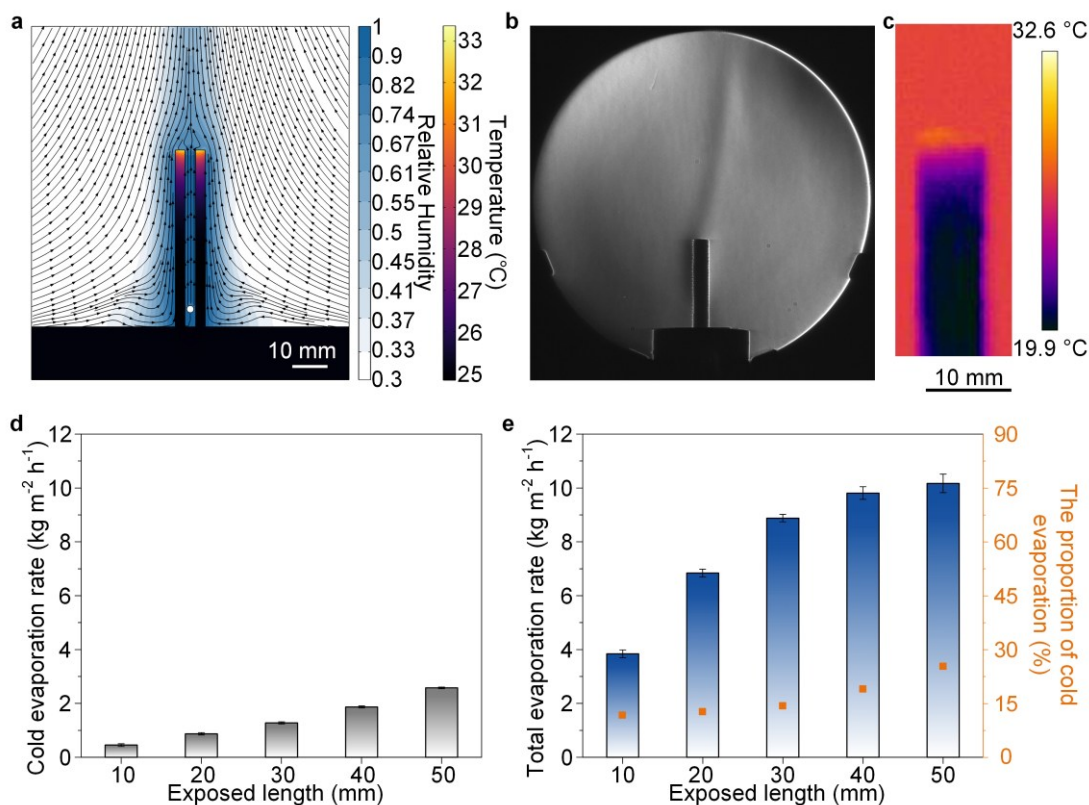


**Fig.S28** Key simulation and performance data for CPCGG under 1-Sun illumination. (a) Simulated distribution of gas streamlines, temperature, and relative humidity. (b) Schlieren image of CPCGG after 1 hour of 1-Sun irradiation, verifying the presence of chimney-driven flow. (c) Infrared thermal image of CPCGG after 1 hour of 1-Sun irradiation. (d) Cold evaporation rate of CPCGG at different exposed lengths under dark conditions. (e) Total evaporation rate under 1-Sun and corresponding proportion of cold evaporation at varying exposed lengths.

### S18. Evaporation rate and energy utilization efficiency at the 9 mm diameter of light spot under 1-Sun

The evaporation rate and energy utilization efficiency of CPCG and CPCGG have been measured at the 9 mm diameter of light spot under 1-Sun (Fig. S29). The results demonstrated that the evaporation rate of CPCG and CPCGG is  $5.4 \text{ kg m}^{-2} \text{ h}^{-1}$  and  $7.8 \text{ kg m}^{-2} \text{ h}^{-1}$ , respectively, and the apparent energy utilization efficiency is 168% and 244%, respectively, indicating that the chimney effect can better absorb and utilize ambient energy.

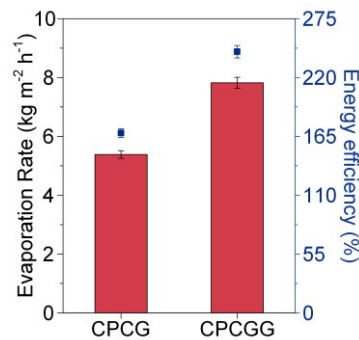


**Fig. S29** Evaporation rate and energy efficiency of CPCG and CPCGG at the 9 mm diameter of light spot under 1-Sun. Three experiments were conducted and the average value was calculated as water evaporation rate and efficiency.

**Table S3.** Comparison of evaporation rate and apparent energy utilization efficiency for evaporators of different shapes under 1-Sun illumination.

Evaporator shape	Evaporation rate ( $\text{kg m}^{-2} \text{ h}^{-1}$ )	Apparent energy utilization efficiency (%)	Reference
Chimney	7.8	244	Our work CPCGG
Cylinder	4.0	139	Ref. <sup>13</sup>
Cattail	4.12	105.8	Ref. <sup>14</sup>
Sunflower	1.51	100.4	Ref. <sup>15</sup>
Arch	2.0	93.5	Ref. <sup>16</sup>
Rose	2.12	91.5	Ref. <sup>17</sup>
Mushroom	1.475	78	Ref. <sup>18</sup>

## S19. Experimental set-up for long-term experiment

In order to test the solar evaporation stability of the 3D printed chimney, the chimney was positioned in the expanded polyethylene foam (EPEF) for floating on the bulk water. The aluminium foil that covered the top surface of EPEF was used to prevent water from penetrating through pores in the EPEF to the top surface which induced evaporation of bulk water. The aluminium foil that covered on the edge of the glass dish was used to prevent direct sunlight irradiation through the glass and the gap between the EPEF and the glass dish to the bulk water. The solar flux at the top surface of the 3D printed chimney was 1-Sun ( $1 \text{ kW}\cdot\text{m}^{-2}$ ), and the evolution of mass with time ( $m(t)$ ) was recorded in-situ by an electronic balance (AH-A+R203K, Shenzhen Anheng weighing device Electronics Co., LTD, China, with measurement range of  $0 \sim 200 \text{ g}$ , and accuracy is  $0.001 \text{ g}$ ) connected to computer (Fig. S30a). In addition, the solar evaporation background without the 3D printing chimney ( $m_v$ ) was also measured under the same conditions (Fig. S30b), and the mass change rate of the solar evaporation background was  $113 \text{ mg/h}$  ( $m_v=113 \text{ mg/h}$ ) during 7 h measurement. Thus, the evolution of solar evaporation rate with time ( $\dot{m}(t)$ ) can be calculated by

$$\dot{m}(t) = \frac{m(t) - m(t - \Delta t)}{A \cdot \Delta t} - \frac{m_v}{A} \quad (\text{SE } 35)$$

where  $\Delta t$  is the time interval of measurement. In this study,  $\Delta t$  was 1 h.

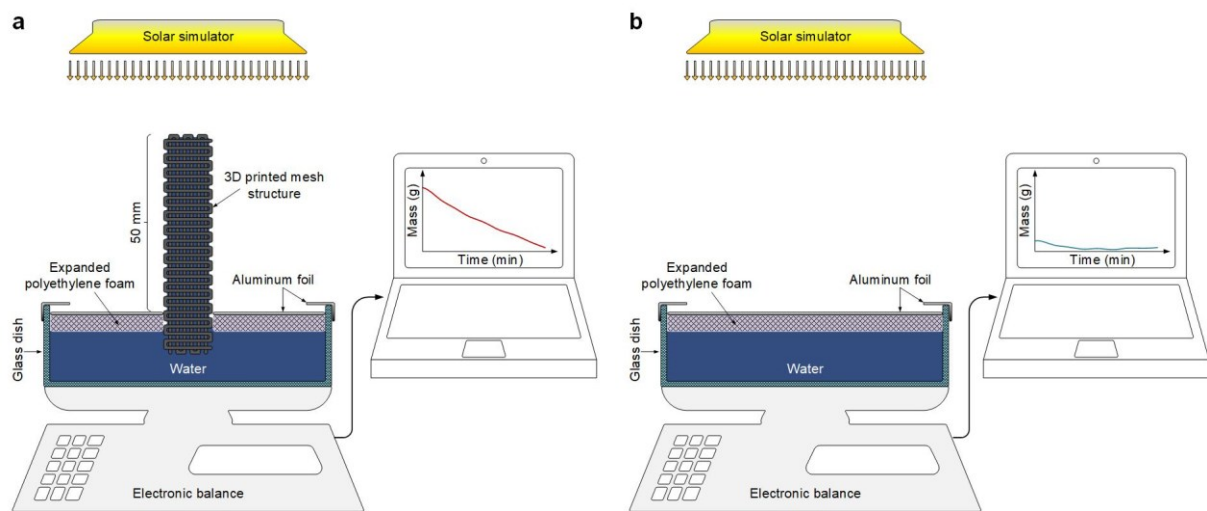


**Fig. S30** Schematic illustration of the experimental set-up for testing solar evaporation stability. (a) Solar evaporation system with the 3D printing chimney. (b) The solar evaporation background without the 3D printed chimney.

## S20. Analysis of internal salt deposition in porous structures under 10 wt% NaCl solution

To assess potential pore clogging during operation, a 48-hour solar evaporation experiment was conducted using CPCGG in a 10 wt% NaCl solution under 1-Sun illumination. Immediately following the test, the sample was freeze-dried to preserve any salt retained within the porous structure for inspection. SEM analysis of the cross-section reveals that NaCl crystals inside the structure are dispersed as nanoscale cuboidal particles. These crystals remain isolated and do not aggregate into larger blocks capable of clogging the micrometer-scale porous network (Figs. S31a and S31b). Higher-magnification SEM images further confirm that the nanoporous regions are not fully obstructed, indicating that salt does not block the hierarchical capillary pathways (Fig. S31c).

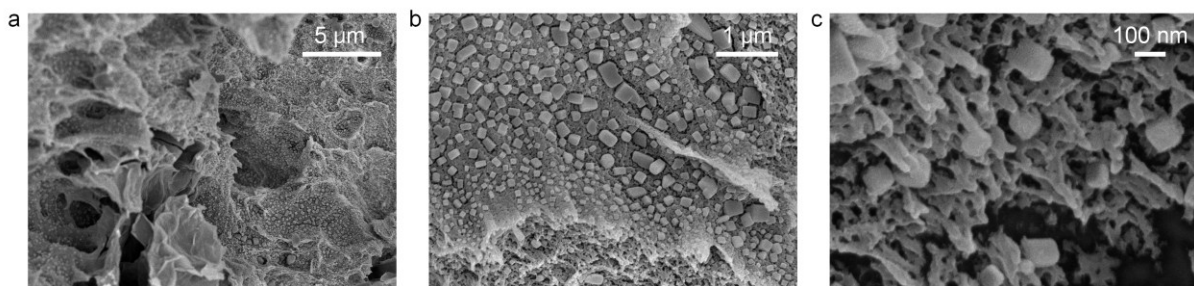


**Fig. S31** SEM images of the CPCGG cross-section at different magnifications after 48-hour evaporation in 10 wt% NaCl under 1-Sun, showing nanoscale, non-clogging salt deposits. (a) 5000x magnification. (b) 20000x magnification. (c) 100000x magnification.

## S21. Simulation results of CPCGG evaporation within the glass cover

To verify the effectiveness of the chimney effect of CPCGG under the high humidity environment within the glass cover, relevant simulations were conducted. The initial humidity inside the chamber was set to 0.9, with the ambient temperature at 30 °C. The sun irradiated the top of the CPCGG at an intensity of 1000 W m<sup>-2</sup>. Considering the tendency of rising vapor to condense on the glass cover,<sup>19</sup> the convective heat transfer coefficient between the glass cover and the steam was set at 45 W m<sup>-2</sup> K<sup>-1</sup>.

The simulation results demonstrate that even within high humidity environment of the glass cover, the upward movement of hot vapor at the top of the CPCGG can initiate the chimney effect (Fig. S32). Furthermore, moisture content within the chamber is distributed unevenly, peaking at the evaporation front. As the vapor raises and diffuses, its moisture concentration gradually diminishes. Upon contacting with the glass cover, vapor tends to condense into water droplets, resulting in a decreased moisture concentration near the glass cover. This drier air can

then circulate back to the surface of the CPCGG *via* the chimney effect, facilitating the absorption and utilization of environmental energy, and thus promoting the evaporation process.

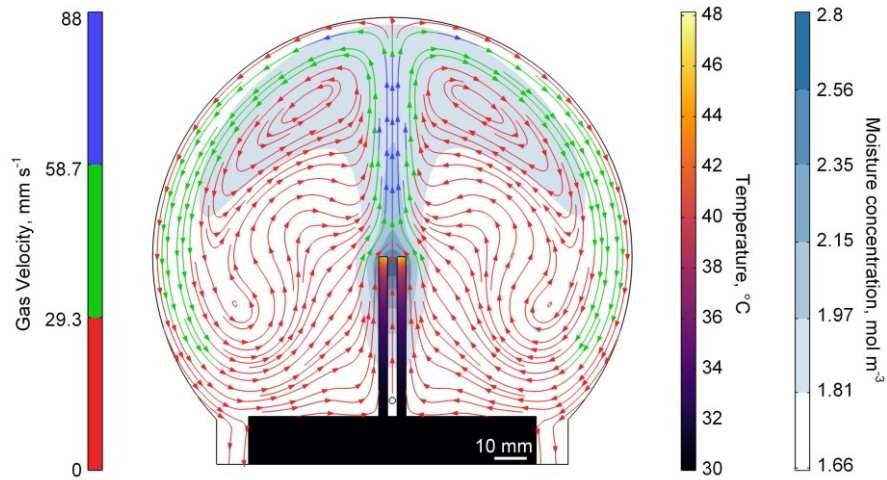


**Fig. S32** Simulation results of CPCGG within the glass cover after reaching steady state.

## S22. Setup for fresh water production from real seawater

In the experiment of clean water production from real seawater, five CPCGG chimneys were installed in the EPEF in an array mode for floating on the real seawater. The distance between four corners of the array and the central CPCGG was 2 cm (Fig. S33). Considering that each CPCGG had a diameter of 0.85 cm, the minimum distance between the two adjacent CPCGGs was 1.15 cm. In addition, other areas of the EPEF surface were covered by aluminium foil to prevent vapor from escaping through these cracks in the EPEF.

As shown in the Fig. 4a of the manuscript, under solar illumination, water vapor diffuses from these chimneys, then condenses upon contacting the glass cover, which eventually slides into the purified water collector located at the bottom. To reduce secondary evaporation of the purified water, a glass dish filled with tap water was placed outside the bottom purified water collector for cooling purpose. Meanwhile, aluminium foil covered on the expanded polyethylene foam (EPEF) and glass cover prevented water vapor from escaping through these gaps inside the EPEF. Polyimide tape was then utilized to fully seal the gap for further minimizing potential evaporative loss. Additionally, the aluminium foil placed above the tap water was provided to shield sunlight that could illuminate on the tap water and the purified water collector to introduce evaporation there.

The methods for calculating the fresh water yield ( $R_{fy}$ ) of these evaporators are derived from previous works,<sup>20, 21</sup> which is shown as following:

$$R_{fy} = \frac{\Delta m_c}{S_t \cdot t} \quad (\text{SE } 36)$$

where  $\Delta m_c$  is the collected fresh water mass in the closed chamber, respectively.  $S_t$  is the total cross-sectional area of these evaporators, and  $t$  is time.

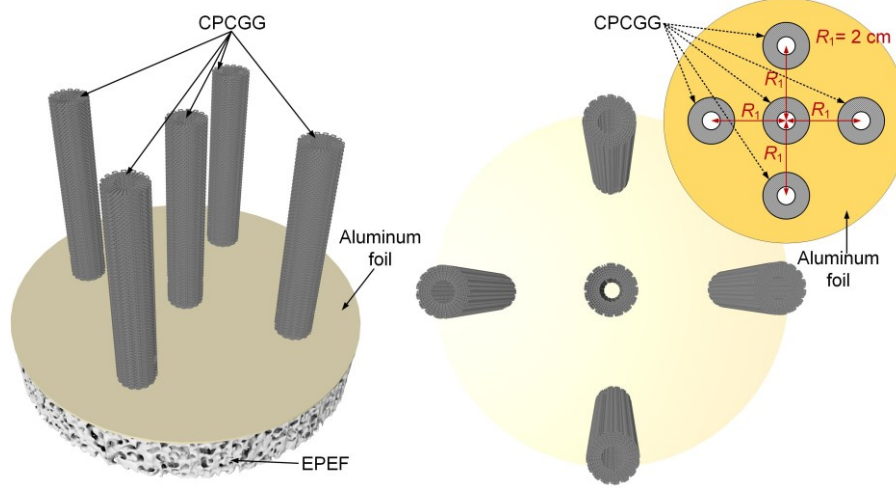


**Fig. S33** The layout of solar evaporator array in the EPEF for clean water production from real seawater.

### S23. Multiple independent experiments and temperature analysis

The multiple independent experiments have been conducted to verify the reliability of our data. For the indoor experiments, four independent indoor experiments have been performed. These indoor experiment lasted for 24 hours. As shown in Fig. S34a, these four independent experiments consistently demonstrate fresh water yield of  $86.7\sim 90.9 \text{ kg m}^{-2} \text{ day}^{-1}$ . The high degree of agreement across these experiments confirms the reliability of our measurements. For the outdoor experiment, three independent outdoor experiments have been conducted—one in *September 2023* (Day O2) with an average solar flux of  $656 \text{ W m}^{-2}$ , and two in *October 2024* (Day O1 and Day O3) with average solar flux intensities of  $307 \text{ W m}^{-2}$  and  $785 \text{ W m}^{-2}$ , respectively. As illustrated in Fig. S34b, in these outdoor experiments, increasing the average solar flux from  $307 \text{ W m}^{-2}$  to  $785 \text{ W m}^{-2}$  leads to an increase in the fresh water yield from  $45.9 \text{ kg m}^{-2} \text{ day}^{-1}$  to  $95.1 \text{ kg m}^{-2} \text{ day}^{-1}$ .

To provide clear evidence of the high fresh water yield in the outdoor experiment, the temperature distribution within the closed chamber and the environment were meticulously measured by eight thermocouples with two data acquisition systems (Fig. S34c).  $T_1$  and  $T_2$  are the top and side temperature of the CPCGG at the corner of the evaporator array, respectively.

$T_3$  and  $T_4$  are the top and side temperature of the CPCGG at the centre of the solar evaporator array, respectively.  $T_5$  and  $T_6$  are the top temperature and side temperature of humid air inside the closed chamber.  $T_7$  is the temperature of inner surface of the glass cover.  $T_8$  is the environment temperature. Therefore, the average temperature of these solar evaporators ( $T_{ac}$ ) can be calculated by:

$$T_{ac} = \frac{T_1 + T_2 + T_3 + T_4}{4} \quad (\text{SE 37})$$

The average temperature of the humid air ( $T_{ah}$ ) in closed chamber can be calculated by:

$$T_{ah} = \frac{T_5 + T_6}{2} \quad (\text{SE 38})$$

The temperature difference between these solar evaporators and the environment ( $\Delta T_{se}$ ), between the humid air in closed chamber and the environment ( $\Delta T_{he}$ ), between the inner surface of the glass cover and the environment ( $\Delta T_{ge}$ ) can be calculated as follows:

$$\Delta T_{se} = T_{ac} - T_8 \quad (\text{SE 39})$$

$$\Delta T_{he} = T_{ah} - T_8 \quad (\text{SE 40})$$

$$\Delta T_{ge} = T_7 - T_8 \quad (\text{SE 41})$$

The experimental results demonstrate that outdoor global sunlight conditions provide more ambient energy to the evaporator, even under lower light intensities ( $<1000 \text{ W m}^{-2}$ ). In the indoor experiments, the solar simulator's output lens, with a diameter of  $\sim 60 \text{ mm}$ , can only offer a limited range of lighting conditions (Fig. S34d). In contrast, the glass cover of our closed chamber used in outdoor experiments has a diameter of  $\sim 150 \text{ mm}$ , allowing sunlight to cover the entire surface of the glass cover and provide more ambient energy. Under indoor conditions with 1-Sun illumination ( $1000 \text{ W m}^{-2}$ ) and an environment temperature ( $T_8$ ) of  $\sim 25 \text{ }^\circ\text{C}$ , the average evaporator temperature ( $T_{ac}$ ) is  $\sim 31 \text{ }^\circ\text{C}$ , yielding a  $\Delta T_{se}$  of  $\sim 6 \text{ }^\circ\text{C}$  (Fig. S34d). However, in outdoor conditions, even with a solar flux of  $253 \text{ W m}^{-2}$  (0.253-Sun) in the morning,  $T_{ac}$  reaches  $\sim 32 \text{ }^\circ\text{C}$  with an environment temperature of  $\sim 26 \text{ }^\circ\text{C}$ , also resulting in a  $\Delta T_{se}$  of  $\sim 6 \text{ }^\circ\text{C}$  (Fig. S34e). This indicates that outdoor global sunlight compensates for the lower direct solar flux by providing additional ambient energy.

Further experimental results show that when global sunlight conditions reached 1-Sun in the outdoor experiment,  $T_{ac}$  increased to  $\sim 51 \text{ }^\circ\text{C}$ , with a  $\Delta T_{se}$  of  $\sim 19 \text{ }^\circ\text{C}$  (Fig. S34f). Additionally, the environment temperatures in these outdoor experiments reach up to  $30\sim 35 \text{ }^\circ\text{C}$  (Figs. S34e and S29f). Given that outdoor experiments with a solar flux of  $253 \text{ W m}^{-2}$  gave rise to sample and environment temperatures similar to those in indoor experiments with  $1000 \text{ W m}^{-2}$

irradiation (Figs. S34d and S34e), it is reasonable to achieve fresh water yield of  $45.9 \text{ kg m}^{-2} \text{ day}^{-1}$ ,  $90.2 \text{ kg m}^{-2} \text{ day}^{-1}$ , and  $95.1 \text{ kg m}^{-2} \text{ day}^{-1}$  in outdoor experiments with average solar flux of  $307 \text{ W m}^{-2}$ ,  $656 \text{ W m}^{-2}$ , and  $785 \text{ W m}^{-2}$ , respectively (Fig. S34b).

Moreover, the glass cover used in the outdoor experiments demonstrates a stronger greenhouse effect than indoor experiments. In the indoor experiments, the temperature difference between the inner surface of the glass cover and the ambient environment ( $\Delta T_{ge}$ ) ranged from  $0.4\sim 2.8 \text{ }^\circ\text{C}$  under 1-Sun (Fig. S34g). However, in the outdoor experiments,  $\Delta T_{ge}$  reached  $8.8 \text{ }^\circ\text{C}$  and  $12.7 \text{ }^\circ\text{C}$  during Day O1 and Day O3, respectively (Fig. S34g). This stronger greenhouse effect indicates that the glass cover retains more latent heat released during the condensation process in outdoor experiment. For instance, the temperature difference between the humid air inside the closed chamber and the ambient environment ( $\Delta T_{he}$ ) reached  $13.7 \text{ }^\circ\text{C}$  and  $20.0 \text{ }^\circ\text{C}$  during Day O1 and Day O3 of outdoor experiment, respectively (Fig. S34g), which are higher than that of  $5.6\sim 6.8 \text{ }^\circ\text{C}$  in the indoor experiments (Fig. S34g). These results indicate that the stronger greenhouse effect in the outdoor experiments significantly facilitates evaporation compared to the indoor experiments. The simulation results show that the chimney effect is still effective even in the closed chamber (see Section S22 and Fig. S33 in the Supplementary Information), which promotes the heat trapped in the humid air to flow back to the surface of the evaporator, and promotes the further increase of the evaporator temperature. Additionally, the experiment results have also shown that the tilted sunlight increases the evaporation rate (Fig. 3a in the manuscript).

In conclusion, the experiment results have provided clear evidence supporting the fresh water yield of these evaporators observed in outdoor experiments. This can be attributed to more ambient energy absorbed from the global sunlight conditions *via* the chimney effect, higher environment temperatures, varying solar incidence angles, and the enhanced greenhouse effect. Moreover, these independent indoor and outdoor experiments confirm the reliability of the data.

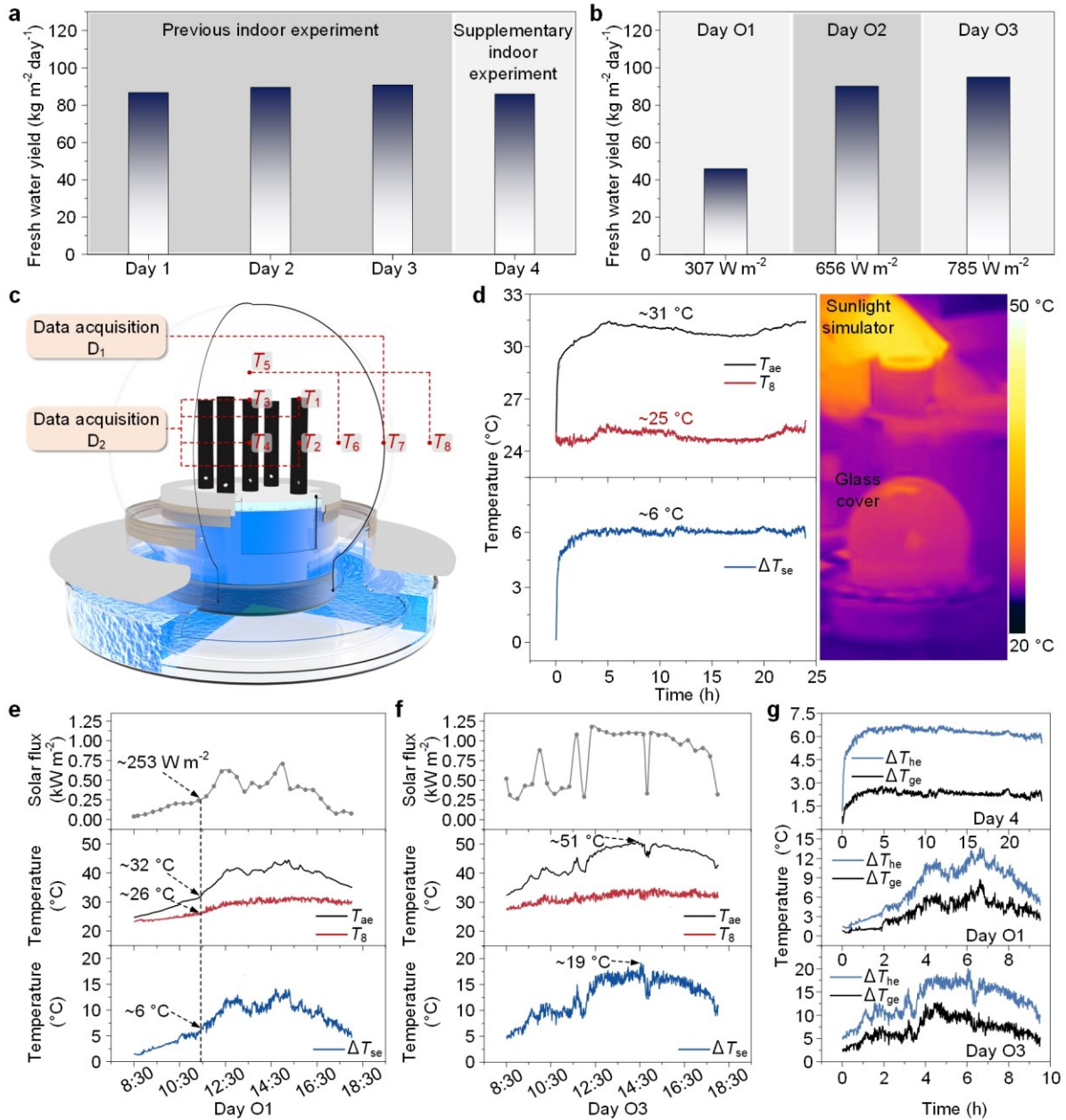


**Fig. S34** Seawater desalination and temperature analysis for indoor and outdoor experiments. (a) Fresh water yield of these evaporators within the closed chamber under indoor 1-Sun illumination for 24 h with four independent tests. (b) Fresh water yield in three independent outdoor experiments with different average solar flux. (c) Schematic diagram of temperature measure system. (d) The temperature distribution and infrared image in the indoor experiment of Day 4. The measured solar flux and temperature distribution during outdoor experiment of (e) Day O1 and (f) Day O3. (g) Comparison of  $\Delta T_{he}$  and  $\Delta T_{ge}$  among indoor experiment and two outdoor experiments, including Day 4, Day O1 and Day O3.

## S24 Analysis of potential scaling caused by multivalent ions such as $\text{Ca}^{2+}$ and $\text{Mg}^{2+}$

To investigate potential scaling caused by multivalent ions such as  $\text{Ca}^{2+}$  and  $\text{Mg}^{2+}$  during long-term desalination, we conducted a 48-hour solar evaporation test using CPCGG with real seawater under 1-Sun illumination. After the test, the sample was freeze-dried to preserve any salt or scale deposits within the structure, followed by SEM and EDS mapping analyses.

The results show only a small amount of salt crystallization within the CPCGG structure after 48 hours of continuous operation (Fig. S35a). The EDS mapping further revealed that Na and Cl were the dominant elements in the salt crystallization, while the concentrations of Ca, and Mg were extremely low and below the detection limit (Fig. S35b). Consequently, Ca and Mg were not detected, indicating that scaling by multivalent ions ( $\text{Ca}^{2+}$  and  $\text{Mg}^{2+}$ ) did not occur under these test conditions. Additionally, these salt crystals were easily removed by rinsing with deionized water, suggesting that no strong or irreversible scaling occurred (Figs. S35c and S35d). These results indicate that CPCGG exhibits excellent resistance to  $\text{Ca}^{2+}$  and  $\text{Mg}^{2+}$  scaling during real seawater desalination under long-term solar exposure.

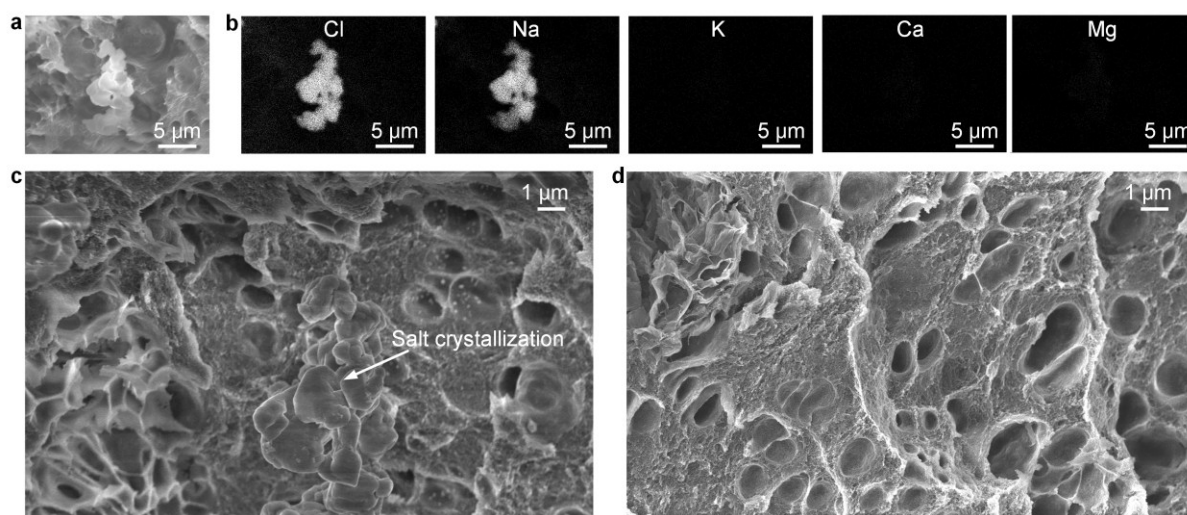


**Fig. S35** Characterization of CPCGG after 48 hours of solar evaporation in real seawater under 1-Sun illumination. (a) SEM image of the internal structure after the 48-hour test. (b) EDS mapping of salt crystallization. It confirms Na and Cl are the dominant elements in the deposits, with negligible levels of K, Ca, and Mg, indicating no evidence of multivalent ion scaling. (c) Salt crystallization observed within the porous structure post-operation. (d) Microstructure of CPCGG after rinsing with deionized water, showing no residual scaling.

## S25. Rejection of antibiotics in pharmaceutical wastewater

The pharmaceutical wastewater contains antibiotics, which poses significant concern to public health and aquatic lives if they are continuously discharged to local environment. Our system is strategically engineered to segregate and recuperate harmful pollutants, thereby facilitating an environmentally sustainable approach to wastewater treatment. As showed by Fig. S36, antibiotic concentrations in purified water produced by CPCGG in solar evaporation were below detection limits ( $0.01 \text{ mg L}^{-1}$ ), which were far less than the original concentrations in pharmaceutical wastewater ( $1000 \text{ mg L}^{-1}$ ), confirming the extremely high rejection rate of  $>99.999\%$  by CPCGG. The rejection rate ( $R_a$ ) is calculated as follows:

$$R_a = \left(1 - \frac{C_p}{C_f}\right) \cdot 100\% \quad (\text{SE } 42)$$

where  $C_p$  and  $C_f$  represent antibiotic concentrations in purified water and pharmaceutical wastewater, respectively.

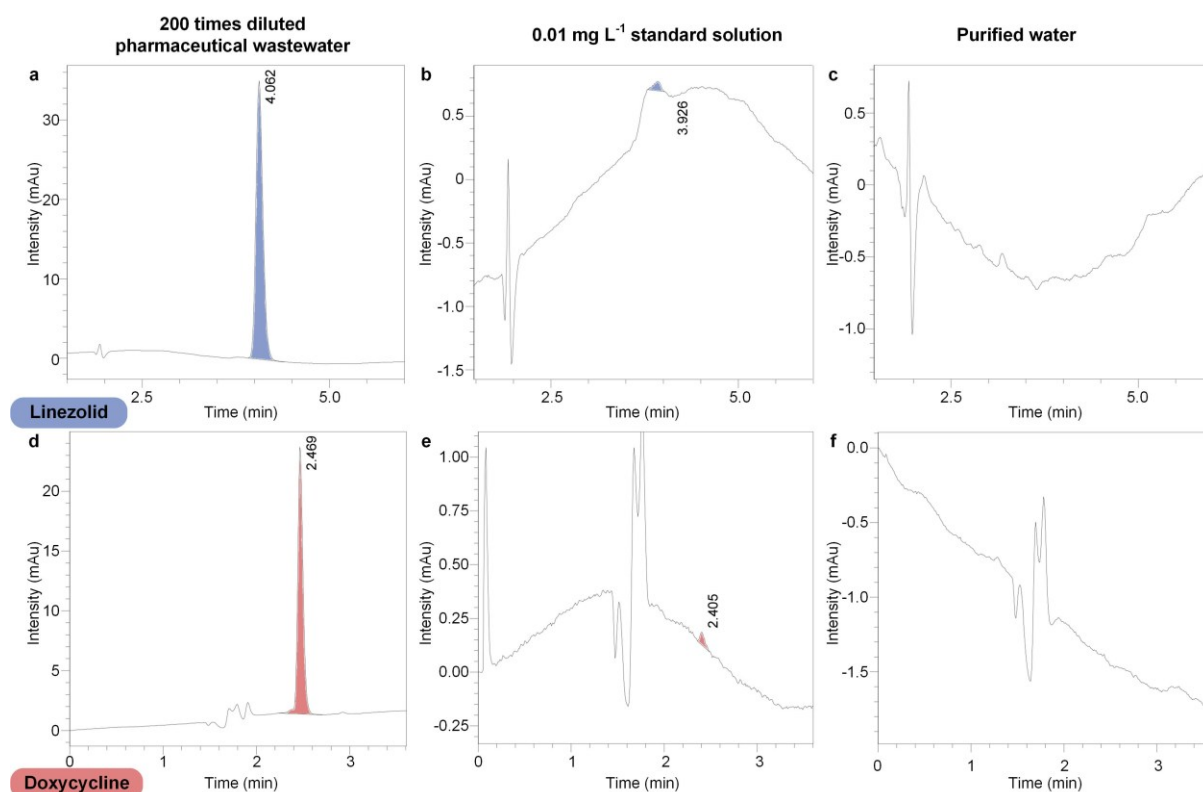


**Fig. S36** Characterization of antibiotic concentrations. The HPLC chromatogram of linezolid in (a) 200 times diluted pharmaceutical wastewater, (b)  $0.01 \text{ mg L}^{-1}$  standard solution, and (c) the collected purified water. Doxycycline in (d) 200 times diluted pharmaceutical wastewater, (e)  $0.01 \text{ mg L}^{-1}$  standard solution, and (f) the collected purified water.

**Table S4.** Detection methods for antibiotics.

Antibiotics	Mobile phase A	Mobile Phase B	Volume ratio (Vol%)	Wavelength (nm)	Reference
Linezolid	Water and Methanol (50:50 by volume)	Na	Na	254	Ref. <sup>22</sup>
Doxycycline	0.1% TFA in water	0.1% TFA in acetonitrile	60:40	360	Ref. <sup>23</sup>

## S26. Management of real pharmaceutical wastewater

In order to test the durability of the CPCGG in the management of real pharmaceutical wastewater, a single CPCGG was floated on the surface of the real pharmaceutical wastewater by tightly positioning it in one layer of aluminium foil (which also shields the bulk water surface from evaporation). The solar flux at the top surface of the 3D printed chimney was 1-Sun (1 kW m<sup>-2</sup>), and the evolution of mass with time was recorded in-situ by an electronic balance connected to computer (Fig. S37a). The water removal ratio ( $m_{\text{wr}}$ ) of the real pharmaceutical wastewater (Fig. S37b) could be calculated by:

$$m_{\text{wr}} = \frac{\Delta m_{\text{total}}}{m_{\text{original}}} \cdot 100\% \quad (\text{SE 43})$$

where  $\Delta m_{\text{total}}$  is the total mass of evaporation, and  $m_{\text{original}}$  is the initial total mass of the real pharmaceutical wastewater.

To evaluate fouling behaviour and reusability, a single CPCGG evaporator was used to remove approximately 40% of water from pharmaceutical wastewater under indoor 1-Sun illumination (Figs. S37a and S37b). Reusability was assessed over five consecutive cycles, with each cycle stopping at ~40% water removal, followed by cleaning of the evaporator. The results show that CPCGG fully recovered its performance in all five cycles (Fig. S37b), confirming its reusability.

To further investigate potential fouling, the CPCGG was freeze-dried after the treatment of 40% of wastewater, and analysed using SEM and EDS mapping (Figs. S37c and S37d). The results revealed only a small amount of foulants deposited within the structure, which did not block the internal hierarchical water channels. In addition, the foulant is mainly composed of potassium instead of calcium and magnesium, making the cleaning and restoration of

performance easy. These results confirm the CPCGG's strong antifouling capability and its suitability for repeated use in treating organic-rich pharmaceutical wastewater.

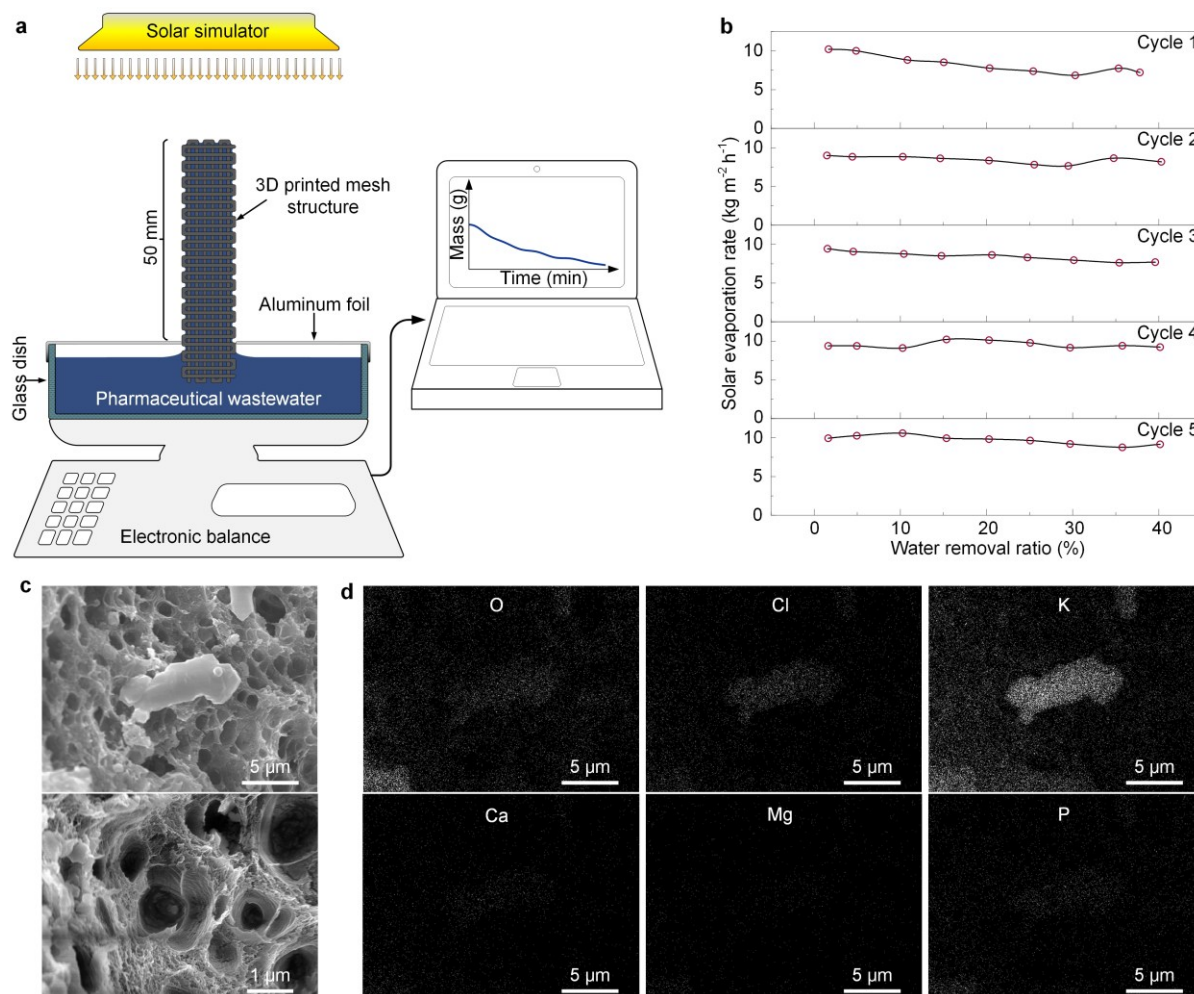


**Fig. S37** Performance of a single CPCGG evaporator treating pharmaceutical wastewater. (a) Schematic illustration of the experimental setup. (b) Evaporation rate as a function of water removal ratio. Each experiment was terminated at ~40% water removal, followed by cleaning of the evaporator. Five consecutive cycles were conducted. (c) SEM images and (d) EDS mapping of the CPCGG after ~40% water removal, showing minor foulant deposition without blockage of internal hierarchical channels.

## Reference

1. Y.-W. Ju and G.-Y. Oh, *Korean J. of Chemical Eng.*, 2017, **34**, 2731-2737.
2. B. Sivaranjini, R. Mangaiyarkarasi, V. Ganesh and S. Umadevi, *Sci. Rep.*, 2018, **8**, 8891.

3. R. Al-Gaashani, A. Najjar, Y. Zakaria, S. Mansour and M. A. Atieh, *Ceram. Int.*, 2019, **45**, 14439-14448.
4. L. Zhou, Y. Tan, D. Ji, B. Zhu, P. Zhang, J. Xu, Q. Gan, Z. Yu and J. Zhu, *Sci. Adv.*, 2016, **2**, e1501227.
5. H. Ghasemi, G. Ni, A. M. Marconnet, J. Loomis, S. Yerci, N. Miljkovic and G. Chen, *Nat. Commun.*, 2014, **5**, 4449.
6. K. Bae, G. Kang, S. K. Cho, W. Park, K. Kim and W. J. Padilla, *Nat. Commun.*, 2015, **6**, 10103.
7. A. K. Datta, *J. Food Eng.*, 2007, **80**, 96-110.
8. A. K. Datta, *J. Food Eng.*, 2007, **80**, 80-95.
9. D. Bunjong, N. Pussadee and P. Wattanakasiwich, *J. Phys.: Conf. Ser.*, 2018, **1144**, 012097.
10. X. Zhou, F. Zhao, Y. Guo, B. Rosenberger and G. Yu, *Sci. Adv.*, 2019, **5**, eaaw5484.
11. F. Zhao, X. Zhou, Y. Shi, X. Qian, M. Alexander, X. Zhao, S. Mendez, R. Yang, L. Qu and G. Yu, *Nat. Nanotechnol.*, 2018, **13**, 489-495.
12. T. Encrenaz, *Annu. Rev. Astron. Astr.*, 2008, **46**, 57-87.
13. X. Wu, T. Gao, C. Han, J. Xu, G. Owens and H. Xu, *Sci. Bull.*, 2019, **64**, 1625-1633.
14. C. Zhang, B. Yuan, Y. Liang, L. Yang, L. Bai, H. Yang, D. Wei, W. Wang and H. Chen, *Sol. Energ. Mat. Sol. C.*, 2021, **227**, 111127.
15. P. Sun, W. Zhang, I. Zada, Y. Zhang, J. Gu, Q. Liu, H. Su, D. Pantelic, B. Jelenkovic and D. Zhang, *ACS Appl. Mater. Interfaces*, 2020, **12**, 2171-2179.
16. Z. Xu, X. Ran, D. Wang, M. Zhong and Z. Zhang, *Desalination*, 2022, **525**, 115495.
17. W. Li, Z. Li, K. Bertelsmann and D. E. Fan, *Adv. Mater.*, 2019, **31**, 1900720.
18. N. Xu, X. Hu, W. Xu, X. Li, L. Zhou, S. Zhu and J. Zhu, *Adv. Mater.*, 2017, **29**, 1606762.
19. Y. Liang, D. Che and Y. Kang, *Heat Mass Transfer*, 2007, **43**, 677-686.
20. J. Li, X. Wang, Z. Lin, N. Xu, X. Li, J. Liang, W. Zhao, R. Lin, B. Zhu, G. Liu, L. Zhou, S. Zhu and J. Zhu, *Joule*, 2020, **4**, 928-937.
21. B. Yang, Z. Zhang, P. Liu, X. Fu, J. Wang, Y. Cao, R. Tang, X. Du, W. Chen, S. Li, H. Yan, Z. Li, X. Zhao, G. Qin, X. Q. Chen and L. Zuo, *Nature*, 2023, **622**, 499-506.
22. C. Fang, O. Garcia-Rodriguez, C. Shang, J. Imbrogno, T. M. Swenson, O. Lefebvre and S. Zhang, *J. Membr. Sci.*, 2023, **676**, 121582.
23. A. C. Kogawa and H. R. Salgado, *J. Chromatogr. Sci.*, 2013, **51**, 919-925.